

# Stabilizing even-parity chiral superconductivity in $\text{Sr}_2\text{RuO}_4$

Han Gyeol Suh,<sup>1</sup> Henri Menke,<sup>2</sup> P. M. R. Brydon,<sup>2</sup> Carsten Timm,<sup>3</sup> Aline Ramires,<sup>4,5,6,\*</sup> and Daniel F. Agterberg<sup>1</sup>

<sup>1</sup>*Department of Physics, University of Wisconsin, Milwaukee, Wisconsin 53201, USA*

<sup>2</sup>*Department of Physics and MacDiarmid Institute for Advanced Materials and Nanotechnology, University of Otago, P.O. Box 56, Dunedin 9054, New Zealand*

<sup>3</sup>*Institute of Theoretical Physics and Würzburg-Dresden Cluster of Excellence ct.qmat, Technische Universität Dresden, D-01062 Dresden, Germany*

<sup>4</sup>*Max Planck Institute for the Physics of Complex Systems, D-01187 Dresden, Germany*

<sup>5</sup>*ICTP-SAIFR, International Centre for Theoretical Physics,*

*South American Institute for Fundamental Research, São Paulo, SP, 01140-070, Brazil*

<sup>6</sup>*Instituto de Física Teórica, Universidade Estadual Paulista, São Paulo, SP 01140-070, Brazil*  
(Dated: April 9, 2024)

Strontium ruthenate ( $\text{Sr}_2\text{RuO}_4$ ) has long been thought to host a spin-triplet chiral  $p$ -wave superconducting state. However, the singletlike response observed in recent spin-susceptibility measurements casts serious doubts on this pairing state. Together with the evidence for broken time-reversal symmetry and a jump in the shear modulus  $c_{66}$  at the superconducting transition temperature, the available experiments point towards an even-parity chiral superconductor with  $k_z(k_x \pm ik_y)$ -like  $E_g$  symmetry, which has consistently been dismissed based on the quasi-two-dimensional electronic structure of  $\text{Sr}_2\text{RuO}_4$ . Here, we show how the orbital degree of freedom can encode the two-component nature of the  $E_g$  order parameter, allowing for a local orbital-antisymmetric spin-triplet state that can be stabilized by on-site Hund's coupling. We find that this exotic  $E_g$  state can be energetically stable once a complete, realistic three-dimensional model is considered, within which momentum-dependent spin-orbit coupling terms are key. This state naturally gives rise to Bogoliubov Fermi surfaces.

*Introduction.* Based on early Knight shift [1], polarized neutron scattering [2], muon-spin-resonance [3], and polar Kerr measurements [4],  $\text{Sr}_2\text{RuO}_4$  has been widely thought to support a spin-triplet chiral  $p$ -wave superconducting state with  $E_u$  symmetry [5–21]. This proposed state has had difficulty reconciling other experimental results [21], including the absence of chiral edge currents [22], thermal transport consistent with a nodal state [23–25], apparent Pauli-limiting effects for in-plane fields [26], and the failure to observe a cusplike behavior of the critical temperature under nematic strain [27, 28]. Plausible explanations for each of these inconsistencies have nevertheless been presented [21, 29, 30]. Recently, however, the Knight shift has been revisited [31, 32] and, contrary to earlier results, a relatively large reduction of the Knight shift for in-plane fields in the superconducting state has been observed. This finding cannot be reconciled with the standard spin-triplet chiral  $p$ -wave state [6].

Although it now seems unlikely that  $\text{Sr}_2\text{RuO}_4$  is a spin-triplet chiral  $p$ -wave superconductor, the observation of broken time-reversal symmetry [3, 4, 33] and a jump in the shear modulus  $c_{66}$  [34, 35] at the critical temperature still indicate a multicomponent order parameter [36]. The only other possible multicomponent channel within  $D_{4h}$  symmetry belongs to the  $E_g$  irreducible representation (irrep) [36]. At the Fermi surface, a chiral order parameter in this channel resembles a spin-singlet  $d$ -wave state, which has horizontal line nodes. Such a

state would appear to imply that the dominant pairing instability involves electrons in different  $\text{RuO}_2$  layers, which is difficult to understand in view of the pronounced quasi-two-dimensional nature of the normal state of  $\text{Sr}_2\text{RuO}_4$ . Indeed, no microscopic calculation for  $\text{Sr}_2\text{RuO}_4$  has found a leading weak-coupling  $E_g$  instability [37–39].

In this Rapid Communication, we show that *local* interactions can lead to a weak-coupling instability in the  $E_g$  channel, once we consider a complete three-dimensional (3D) model for the normal state. Physically, this  $E_g$  state is a local (i.e.,  $s$ -wave) orbital-antisymmetric spin-triplet (OAST) state stabilized by on-site Hund's coupling. When the renormalized low-energy Hund's coupling  $J$  becomes larger than the interorbital Hubbard interaction  $U'$ , this channel develops an attractive interaction [40–45]. This pairing instability has been found in dynamical mean-field theory, which predicts it appears in the strong-coupling limit even when the unrenormalized high-energy  $J$  is less than  $U'$  [46], and also in the presence of strong charge fluctuations [47]. Pairing due to this type of interaction was considered for  $\text{Sr}_2\text{RuO}_4$  in Ref. [40], where an  $A_{1g}$  pairing state was found to be stable. Motivated by the relevance of  $J$  for the normal state of  $\text{Sr}_2\text{RuO}_4$  [48], we revisit the local-pairing scenario. We note that, remarkably, a similar OAST pairing state is believed to be responsible for nematic superconductivity in  $\text{Cu}_x\text{Bi}_2\text{Se}_3$  [49–51]. In the following, we show that an  $E_g$  state can be stabilized over the  $A_{1g}$  state of Ref. [40] by including momentum-dependent spin-orbit coupling (SOC) corresponding to interlayer spin-dependent hopping with a hopping integral on the order of 10 meV. This small value leaves the quasi-two-dimensional nature of the band structure in-

\* Present address: Paul Scherrer Institut, CH-5232 Villigen, Switzerland

tact. Moreover, we use the concept of superconducting fitness [52, 53] to understand the importance of this term in stabilizing the  $E_g$  state. Finally, we show that this chiral multiorbital  $E_g$  state will display Bogoliubov Fermi surfaces [54, 55], instead of line nodes.

*Normal-state Hamiltonian.* An accurate description of the normal-state Hamiltonian is crucial for understanding superconductivity in the weak-coupling limit. Our starting point is a tight-binding parametrization of the normal-state Hamiltonian that includes all terms allowed by symmetry [56]. To determine the magnitude of each term, we carry out a fit to the density-functional theory (DFT) results of Veenstra *et al.* [57]. Details on the numerical procedures are provided in the Supplemental Material (SM) [58]. However, angle-resolved photoemission spectroscopy (ARPES) measurements [48, 62] suggest that some DFT parameters differ appreciably from the measured values, in particular the SOC strengths [57]. We therefore allow the SOC parameters to vary in order to understand how they affect the leading superconducting instability, under the constraint that the Fermi surfaces do not differ significantly from the DFT predictions and are hence still qualitatively in accordance with the ARPES results.

The relevant low-energy degrees of freedom (DOF) are the electrons in the  $t_{2g}$ -orbital manifold  $d_{yz}$ ,  $d_{xz}$ , and  $d_{xy}$  of Ru. Using the spinor operator  $\Phi_{\mathbf{k}}^\dagger = (c_{\mathbf{k},yz\uparrow}^\dagger, c_{\mathbf{k},yz\downarrow}^\dagger, c_{\mathbf{k},xz\uparrow}^\dagger, c_{\mathbf{k},xz\downarrow}^\dagger, c_{\mathbf{k},xy\uparrow}^\dagger, c_{\mathbf{k},xy\downarrow}^\dagger)$ , where  $c_{\mathbf{k},\gamma\sigma}^\dagger$  creates an electron with momentum  $\mathbf{k}$  and spin  $\sigma$  in orbital  $\gamma$ , we construct the most general three-orbital single-particle Hamiltonian as  $H_0 = \sum_{\mathbf{k}} \Phi_{\mathbf{k}}^\dagger \hat{H}_0(\mathbf{k}) \Phi_{\mathbf{k}}$  with

$$\hat{H}_0(\mathbf{k}) = \sum_{a=0}^8 \sum_{b=0}^3 h_{ab}(\mathbf{k}) \lambda_a \otimes \sigma_b, \quad (1)$$

where the  $\lambda_a$  are Gell-Mann matrices encoding the orbital DOF and the  $\sigma_b$  are Pauli matrices encoding the spin ( $\lambda_0$  and  $\sigma_0$  are unit matrices), and  $h_{ab}(\mathbf{k})$  are even functions of momentum. Time-reversal and inversion symmetries allow only for 15  $h_{ab}(\mathbf{k})$  functions to be finite. The explicit form of the  $h_{ab}(\mathbf{k})$  functions and the Gell-Mann matrices are given in the SM [58].

*Interactions and superconductivity.* We consider on-site interactions of the Hubbard-Kanamori type [63],

$$\begin{aligned} H_{\text{int}} = & \frac{U}{2} \sum_{i,\gamma,\sigma \neq \sigma'} n_{i\gamma\sigma} n_{i\gamma\sigma'} + \frac{U'}{2} \sum_{i,\gamma \neq \gamma',\sigma,\sigma'} n_{i\gamma\sigma} n_{i\gamma'\sigma'} \\ & + \frac{J}{2} \sum_{i,\gamma \neq \gamma',\sigma,\sigma'} c_{i\gamma\sigma}^\dagger c_{i\gamma'\sigma'}^\dagger c_{i\gamma\sigma'} c_{i\gamma'\sigma} \\ & + \frac{J'}{2} \sum_{i,\gamma \neq \gamma',\sigma \neq \sigma'} c_{i\gamma\sigma}^\dagger c_{i\gamma'\sigma'}^\dagger c_{i\gamma'\sigma} c_{i\gamma\sigma}, \end{aligned} \quad (2)$$

where  $c_{i\gamma\sigma}^\dagger$  ( $c_{i\gamma\sigma}$ ) creates (annihilates) an electron at site  $i$  in orbital  $\gamma$  with spin  $\sigma$ , and  $n_{i\gamma\sigma} = c_{i\gamma\sigma}^\dagger c_{i\gamma\sigma}$ . The

Irrep	$[a, b]$	Orbital	Spin	Interaction $g$
$A_{1g}$	$[0, 0]$	symmetric	singlet	$U + 2J$
	$[8, 0]$	symmetric	singlet	$U - J$
	$[4, 3]$	antisymmetric	triplet	$U' - J$
	$[5, 2] - [6, 1]$	antisymmetric	triplet	$U' - J$
$A_{2g}$	$[5, 1] + [6, 2]$	antisymmetric	triplet	$U' - J$
$B_{1g}$	$[7, 0]$	symmetric	singlet	$U - J$
	$[5, 2] + [6, 1]$	antisymmetric	triplet	$U' - J$
$B_{2g}$	$[1, 0]$	symmetric	singlet	$U' + J$
	$[5, 1] - [6, 2]$	antisymmetric	triplet	$U' - J$
$E_g$	$\{[2, 0], [3, 0]\}$	symmetric	singlet	$U' + J$
	$\{[4, 1], [4, 2]\}$	antisymmetric	triplet	$U' - J$
	$\{[6, 3], -[5, 3]\}$	antisymmetric	triplet	$U' - J$

TABLE I. All even-parity local gap functions classified by irreps of the point group  $D_{4h}$ . Here,  $[a, b]$  corresponds to the parametrization of the gap matrix as  $\lambda_a \otimes \sigma_b (i\sigma_2)$ . The other columns give the orbital and spin character, as well as the interaction  $g$  for each superconducting state derived from the Hubbard-Kanamori interaction  $H_{\text{int}}$  in Eq. (2). Note that the two components of the  $E_g$  order parameters can stem from the orbital DOF, as for  $\{[2, 0], [3, 0]\}$  and  $\{[6, 3], -[5, 3]\}$ , or from the spin DOF, as for  $\{[4, 1], [4, 2]\}$ .

first two terms describe repulsion ( $U, U' > 0$ ) between electrons in the same and in different orbitals, respectively. The third and fourth terms represent the Hund's exchange interaction and pair-hopping interactions respectively. We take  $J = J'$  [63], where  $J > 0$  is expected for  $\text{Sr}_2\text{RuO}_4$ . In the context of  $\text{Sr}_2\text{RuO}_4$ ,  $H_{\text{int}}$  is usually taken as the starting point for the calculation of the spin- and charge-fluctuation propagators which enter into the effective interaction [16, 19]. Here, we take a different approach [40, 43] by directly decoupling the interaction in the Cooper channel, which, for  $U' - J < 0$ , yields an attractive interaction for on-site pairing in an OAST state. This scenario has previously been applied to a two-dimensional model of  $\text{Sr}_2\text{RuO}_4$ , predicting an OAST  $A_{1g}$  state [40]. Although a strong-coupling instability towards an OAST  $E_g$  state in the absence of SOC has been predicted in Ref. [47], the superconductivity in  $\text{Sr}_2\text{RuO}_4$  is likely in the weak-coupling regime [21]. It is therefore important to understand if an OAST  $E_g$  state can be the leading instability in this limit.

In the spirit of Ref. [43], we treat  $H_{\text{int}}$  as a renormalized low-energy effective interaction. We tabulate the allowed local gap functions, their symmetries, and the interactions in the respective pairing channels in Table I. Here, we adopt the common assumption of on-site rotational symmetry, which stipulates  $U = U' + 2J$  [63]. This choice implies that all the OAST channels have the

same attractive pairing interaction, which highlights the role of the normal-state Hamiltonian in selecting the most stable state. However, since the Ru sites have  $D_{4h}$  symmetry and not the assumed full rotational symmetry, the interaction strengths for the different pairing channels are generally different. Our results should therefore be interpreted as providing a guide to which superconducting states this form of attractive interaction can give rise to.

We write a free-energy expansion up to second order in the superconducting order parameter given by the gap matrices  $\hat{\Delta}_i = \Delta_i \lambda_{a_i} \otimes \sigma_{b_i} (i\sigma_2)$ ,

$$\mathcal{F} = \frac{1}{2} \sum_i \frac{1}{g_i} \text{Tr} [\hat{\Delta}_i^\dagger \hat{\Delta}_i] - \frac{k_B T}{2} \sum_{\mathbf{k}, \omega, i, j} \text{Tr} [\hat{\Delta}_i \hat{G} \hat{\Delta}_j^\dagger \hat{G}], \quad (3)$$

where  $i$  and  $j$  sum over all channels of a chosen irrep,  $g_i$  are the corresponding interaction strengths from Table I,  $\omega_m = (2m+1)\pi k_B T$  are the fermionic Matsubara frequencies, and  $\hat{G} = (i\omega_m - \hat{H}_0)^{-1}$  and  $\hat{G} = (i\omega_m + \hat{H}_0^T)^{-1}$  are the normal-state Green's functions. Nontrivial solutions of the coupled linearized gap equations obtained from  $\partial \mathcal{F} / \partial \Delta_i^* = 0$  give the critical temperature  $T_c$  and the linear combination of the  $\hat{\Delta}_i$  corresponding to the leading instability. We include all channels in a chosen irrep, not just the attractive ones (see Table I). In evaluating the last term in Eq. (3), we keep only intraband contributions; although the inclusion of interband terms will shift  $T_c$ , this effect is negligible in the weak-coupling regime, as discussed in detail in the SM [58].

**Results.** Weak-coupling OAST pairing states for an attractive Hund's interaction require nonvanishing SOC [43, 44, 53]. As described in the SM [58], SOC appears in five terms in the Hamiltonian  $\hat{H}_0(\mathbf{k})$  in Eq. (1), representing a large parameter space to explore. We shall focus on the effects of the following terms: the  $z$  component of the atomic SOC,  $h_{43} = \eta_z$ ; the in-plane atomic SOC,  $h_{52} - h_{61} = \eta_\perp$ ; and the momentum-dependent SOC associated with the interlayer hopping amplitude  $t_{56z}^{\text{SOC}}$  between the  $d_{xy}$  and the  $d_{xz}$  and  $d_{yz}$  orbitals,  $\{h_{53}, h_{63}\} = 8t_{56z}^{\text{SOC}} \sin(k_z c/2) \{\cos(k_x a/2) \sin(k_y a/2), -\sin(k_x a/2) \cos(k_y a/2)\}$ . Here, we will ignore the anisotropy of the atomic SOC and set  $\eta_z = \eta_\perp = \eta$ . We have carried out a cursory exploration of the larger SOC parameter space and find that varying the other parameters within reasonable ranges such that the Fermi surfaces do not significantly deviate from the DFT predictions has little effect on the leading instability.

Figure 1(a) shows the phase diagram as a function of the atomic SOC  $\eta$  and the momentum-dependent SOC, parametrized by  $t_{56z}^{\text{SOC}}$ . We find leading instabilities in the  $A_{1g}$  and  $E_g$  channels.  $A_{2g}$  and  $B_{2g}$  states are not competitive anywhere in the phase diagram. A  $B_{1g}$  state is sometimes found as a subleading instability. The  $E_g$  solution is dominated by the  $\{[6, 3], -[5, 3]\}$  channel and is stabilized for  $t_{56z}^{\text{SOC}} \gtrsim \eta/4$ . Under the constraint of realistic Fermi surfaces, the  $E_g$  state can be stabilized for

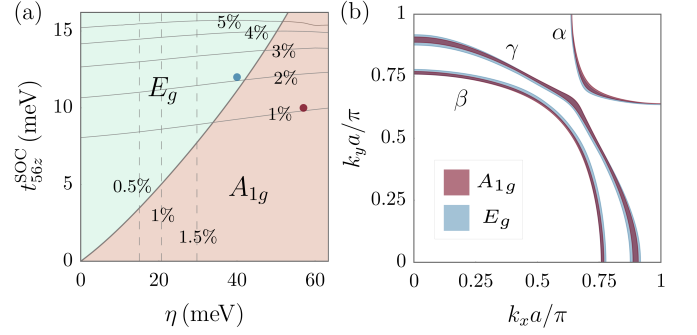


FIG. 1. (a) Phase diagram showing the stability of  $A_{1g}$  and  $E_g$  pairing states as a function of the SOC parameters  $\eta$  and  $t_{56z}^{\text{SOC}}$ . The vertical dashed lines indicate the minimum distance between two Fermi surfaces. Percentages are defined as fractions of  $2\pi/a$ . For small  $\eta$ , the separation between the  $\beta$  and  $\gamma$  bands becomes too small, in view of the ARPES data [48]. The thin solid lines indicate the maximum variation of the Fermi surface along the  $k_z$  direction. For large  $t_{56z}^{\text{SOC}}$ , the Fermi surfaces become too dispersive. The blue and magenta dots denote the parameter choices for  $E_g$  and  $A_{1g}$  stable solutions used in (b). (b) Fermi-surface shapes, projected onto the  $k_x k_y$  plane, for representative points in the  $A_{1g}$  (red) and  $E_g$  (blue) regions in (a). For  $A_{1g}$ ,  $\eta = 57$  meV and  $t_{56z}^{\text{SOC}} = 10$  meV, while for  $E_g$ ,  $\eta = 40$  meV and  $t_{56z}^{\text{SOC}} = 12$  meV.

$t_{56z}^{\text{SOC}}$  as small as about 5 meV, although this requires a rather small value of the on-site SOC. It is remarkable that such a small energy scale determines the relative stability of qualitatively different pairing states. As shown in Fig. 1(b), the Fermi surfaces for parameters stabilizing  $A_{1g}$  or  $E_g$  states are indeed very similar. The SOC strength remains controversial [48, 57, 62], but here we have shown its importance for the determination of the most stable superconducting state. Our results are a proof of principle that an  $E_g$  superconducting state can be realized in  $\text{Sr}_2\text{RuO}_4$ , even for purely local interactions, once one properly takes into account a complete and plausible 3D model for the normal state.

Figure 2 displays the projected gaps at the Fermi surfaces for representative  $A_{1g}$  and  $E_g$  states. Note that in both cases the gap magnitude on the  $\alpha$  sheet is very small, whereas the gaps on the  $\beta$  and  $\gamma$  sheets are comparable. This shows that we cannot simply identify the  $\gamma$  band [64] or the pair of almost one-dimensional  $\alpha$  and  $\beta$  bands [16] as the dominant ones for superconductivity [19].

It is possible to understand why these SOC terms stabilize the respective ground states based on the notion of superconducting fitness [52, 53]. In particular, it has been shown for two-band superconductors that if the quantity  $\tilde{F}_A(\mathbf{k}) = \tilde{H}_0(\mathbf{k})\hat{\Delta}(\mathbf{k}) + \hat{\Delta}(\mathbf{k})\tilde{H}_0^*(-\mathbf{k})$  is zero there is no intraband pairing and hence no weak-coupling instability [here,  $\tilde{H}_0(\mathbf{k})$  corresponds to  $\hat{H}_0(\mathbf{k})$  with  $h_{00}(\mathbf{k})$  set to zero]. Hence, adding terms to the normal-state Hamiltonian such that  $\tilde{F}_A(\mathbf{k})$  becomes nonzero for a particular gap function turns on a weak-coupling instability in this

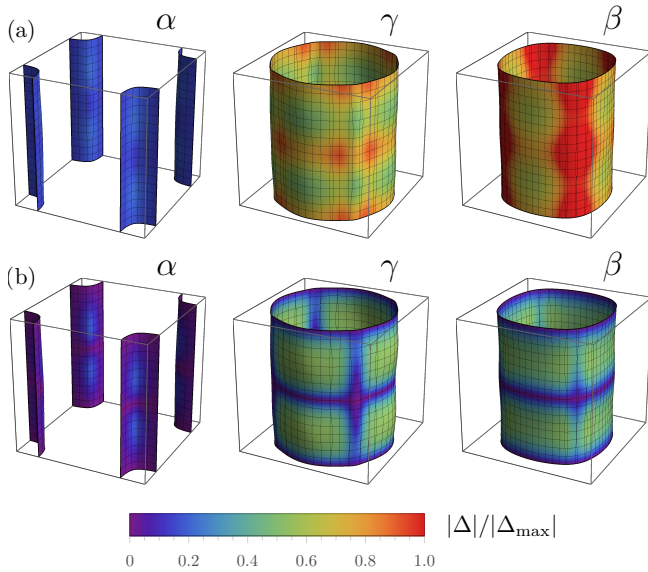


FIG. 2. Projected gaps at the Fermi surfaces for a representative (a)  $A_{1g}$  and (b) chiral  $E_g$  state in the first Brillouin zone. Parameters are the same as in Fig. 1 (b). The color code is normalized to the maximum value of the  $A_{1g}$  gap.

channel. The fitness analysis can be extended to our three-orbital model or, alternatively, we can construct an effective two-orbital model valid sufficiently far from the Brillouin-zone diagonals. Applying the fitness argument to the effective two-band model, we find that the on-site SOC  $\eta$  turns on both the  $A_{1g}$  and  $B_{1g}$  pairing channels, whereas the parameter  $t_{56z}^{\text{SOC}}$  turns on the  $E_g$   $\{[6, 3], -[5, 3]\}$  channel, consistent with what we find numerically. Details of the fitness analysis are given in the SM [58].

In view of the Knight-shift experiments [31, 32], it is important to comment on the spin susceptibility associated with the dominant  $E_g$   $\{[6, 3], -[5, 3]\}$  channel. Since it is a spin-triplet state with in-plane spin polarization of the Copper pairs, similar to the familiar chiral  $p$ -wave spin-triplet pairing with a  $\mathbf{d}$ -vector along the  $k_z$  direction, it might naively be expected to show a temperature-independent spin susceptibility for in-plane fields. This is not the case, however, since the even parity of  $E_g$  implies that the intraband pairing potential is a pseudo-spin singlet when expressed in the band basis and the low-energy response to a magnetic field is identical to a true spin singlet. This has been examined numerically for similar pairing states [45, 65], where it was found that only a small fraction of the normal-state spin susceptibility persists at zero temperature in the superconducting state.

*Bogoliubov Fermi surfaces.* An  $E_g$  state is expected to have horizontal line nodes at  $k_z = 0$  and  $2\pi/c$  [21, 36], and it will have vertical line nodes in a time-reversal invariant nematic state [34, 36]. Although recent tunneling measurements have called into question time-reversal

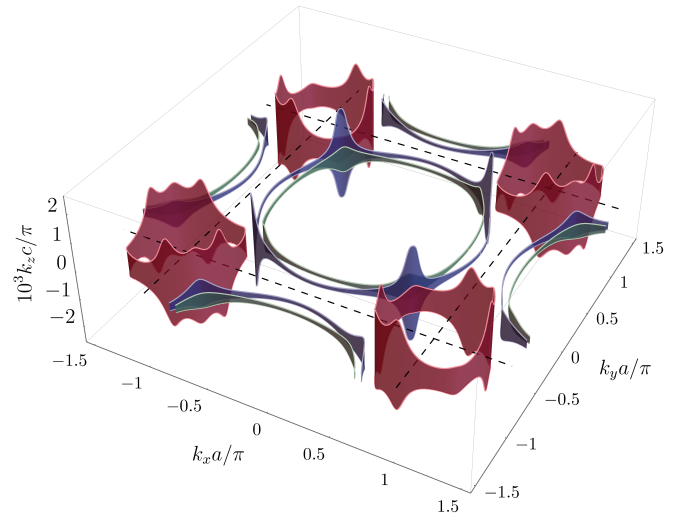


FIG. 3. BFSs for the chiral  $E_g$  state. The Fermi surfaces in red, green, and blue correspond to inflated nodes stemming from the  $\alpha$ ,  $\beta$ , and  $\gamma$  band, respectively.

symmetry breaking in  $\text{Sr}_2\text{RuO}_4$  [66], here we follow the indications of polar Kerr and  $\mu\text{SR}$  experiments [3, 4, 33], and explicitly consider a chiral  $E_g$  state which has no vertical line nodes. It has recently been shown that for an even-parity superconductor that spontaneously breaks time-reversal symmetry, the excitation spectrum is either fully gapped or contains Bogoliubov Fermi surfaces (BFSs) [54, 55]. Indeed, the chiral  $E_g$  state considered here has BFSs, which are shown in Fig. 3. These BFSs are very thin in the direction perpendicular to the normal-state Fermi surface, giving them a ribbon-like appearance that extends along the  $k_z$  axis by about 0.2% of the Brillouin zone. This value is proportional to the gap amplitude, here set to 0.15 meV. While the total residual density of states from the BFSs is not large and may be difficult to observe [67], such a nodal structure implies that some experimental results require reinterpretation. In particular, given that the BFSs extend along the  $k_z$ -axis, the argument that thermal conductivity measurements rule out the  $E_g$  state because it has horizontal line nodes [24] no longer applies. The presence of BFSs may also require a reinterpretation of quasi-particle-interference experiments [68]. We leave a detailed study of experimental consequences of the  $E_g$  OAST state for future work.

*Conclusions.* We have argued that an  $E_g$  order parameter can be a realistic weak-coupling ground state for  $\text{Sr}_2\text{RuO}_4$ , once we consider a complete 3D model for the normal state and interactions of the Hubbard-Kanamori type. Key to our construction are the usually neglected momentum-dependent SOC terms in the normal state. These terms can completely change the nature of the superconducting ground state, despite being so small that they do not significantly change the Fermi surfaces.

Our theory reconciles the recent observation of a singlet-like spin susceptibility with measurements indicating a two-component order parameter and broken time-reversal symmetry.

*Acknowledgments.* The authors thank A. V. Chubukov and B. Ramshaw for useful discussions. H.M. and P.M.R.B. were supported by the Marsden Fund Council from Government funding, managed by Royal Society Te Apārangi. A.R. acknowledges the support of Fundação de Amparo à Pesquisa do Estado de São Paulo (FAPESP) Project No. 2018/18287-8, and Fundação para o Desenvolvimento da UNESP (FUNDUNESP) Process No. 2338/2014-CCP. C.T. acknowledges financial support by the Deutsche Forschungsgemeinschaft through the Collaborative Research Center SFB 1143, Project A04, the Research Training Group GRK 1621, and the Cluster of Excellence on Complexity and Topology in Quantum Matter ct.qmat (EXC 2147).

H.G.S. and H.M. contributed equally to this work.

- 
- [1] K. Ishida, H. Mukuda, Y. Kitaoka, K. Asayama, Z. Q. Mao, Y. Mori, and Y. Maeno, Spin-triplet superconductivity in  $\text{Sr}_2\text{RuO}_4$  identified by  $^{17}\text{O}$  Knight shift, *Nature (London)* **396**, 658–660 (1998).
  - [2] J. A. Duffy, S. M. Hayden, Y. Maeno, Z. Mao, J. Kulda, and G. J. McIntyre, Polarized-neutron scattering study of the cooper-pair moment in  $\text{Sr}_2\text{RuO}_4$ , *Phys. Rev. Lett.* **85**, 5412–5415 (2000).
  - [3] G. M. Luke, Y. Fudamoto, K. M. Kojima, M. I. Larkin, J. Merrin, B. Nachumi, Y. J. Uemura, Y. Maeno, Z. Q. Mao, Y. Mori, H. Nakamura, and M. Sigrist, Time-reversal symmetry-breaking superconductivity in  $\text{Sr}_2\text{RuO}_4$ , *Nature (London)* **394**, 558–561 (1998).
  - [4] J. Xia, Y. Maeno, P. T. Beyersdorf, M. M. Fejer, and A. Kapitulnik, High resolution polar kerr effect measurements of  $\text{Sr}_2\text{RuO}_4$ : Evidence for broken time-reversal symmetry in the superconducting state, *Phys. Rev. Lett.* **97**, 167002 (2006).
  - [5] Y. Maeno, H. Hashimoto, K. Yoshida, S. Nishizaki, T. Fujita, J. G. Bednorz, and F. Lichtenberg, Superconductivity in a layered perovskite without copper, *Nature (London)* **372**, 532–534 (1994).
  - [6] T. M. Rice and M. Sigrist,  $\text{Sr}_2\text{RuO}_4$ : an electronic analogue of  $^3\text{He}$ ? *J. Phys.: Condens. Matter* **7**, L643–L648 (1995).
  - [7] I. I. Mazin and D. J. Singh, Competitions in layered ruthenates: Ferromagnetism versus antiferromagnetism and triplet versus singlet pairing, *Phys. Rev. Lett.* **82**, 4324–4327 (1999).
  - [8] K. Miyake and O. Narikiyo, Model for unconventional superconductivity of  $\text{Sr}_2\text{RuO}_4$ : Effect of impurity scattering on time-reversal breaking triplet pairing with a tiny gap, *Phys. Rev. Lett.* **83**, 1423–1426 (1999).
  - [9] T. Kuwabara and M. Ogata, Spin-triplet superconductivity due to antiferromagnetic spin-fluctuation in  $\text{Sr}_2\text{RuO}_4$ , *Phys. Rev. Lett.* **85**, 4586–4589 (2000).
  - [10] M. Sato and M. Kohmoto, Mechanism of spin-triplet superconductivity in  $\text{Sr}_2\text{RuO}_4$ , *J. Phys. Soc. Jpn.* **69**, 3505–3508 (2000).
  - [11] T. Takimoto, Orbital fluctuation-induced triplet superconductivity: Mechanism of superconductivity in  $\text{Sr}_2\text{RuO}_4$ , *Phys. Rev. B* **62**, R14641–R14644 (2000).
  - [12] T. Nomura and K. Yamada, Roles of electron correlations in the spin-triplet superconductivity of  $\text{Sr}_2\text{RuO}_4$ , *J. Phys. Soc. Jpn.* **71**, 1993–2004 (2002).
  - [13] Y. Yanase and M. Ogata, Microscopic identification of  $D$ -vector in triplet superconductor  $\text{Sr}_2\text{RuO}_4$ , *J. Phys. Soc. Jpn.* **72**, 673–687 (2003).
  - [14] J. F. Annett, G. Litak, B. L. Györfy, and K. I. Wysokiński, Spin-orbit coupling and symmetry of the order parameter in strontium ruthenate, *Phys. Rev. B* **73**, 134501 (2006).
  - [15] Y. Yoshioka and K. Miyake, Pairing mechanism and anisotropy of  $d$ -vector of spin-triplet superconductor  $\text{Sr}_2\text{RuO}_4$ , *J. Phys. Soc. Jpn.* **78**, 074701 (2009).
  - [16] S. Raghu, A. Kapitulnik, and S. A. Kivelson, Hidden quasi-one-dimensional superconductivity in  $\text{Sr}_2\text{RuO}_4$ , *Phys. Rev. Lett.* **105**, 136401 (2010).
  - [17] Q. H. Wang, C. Platt, Y. Yang, C. Honerkamp, F. C. Zhang, W. Hanke, T. M. Rice, and R. Thomale, Theory of superconductivity in a three-orbital model of  $\text{Sr}_2\text{RuO}_4$ , *Europhys. Lett.* **104**, 17013 (2013).
  - [18] J.-W. Huo, T. M. Rice, and F.-C. Zhang, Spin density wave fluctuations and  $p$ -wave pairing in  $\text{Sr}_2\text{RuO}_4$ , *Phys. Rev. Lett.* **110**, 167003 (2013).
  - [19] T. Scaffidi, J. C. Romers, and S. H. Simon, Pairing symmetry and dominant band in  $\text{Sr}_2\text{RuO}_4$ , *Phys. Rev. B* **89**, 220510 (2014).
  - [20] M. Tsuchiizu, Y. Yamakawa, S. Onari, Y. Ohno, and H. Kontani, Spin-triplet superconductivity in  $\text{Sr}_2\text{RuO}_4$  due to orbital and spin fluctuations: Analyses by two-dimensional renormalization group theory and self-consistent vertex-correction method, *Phys. Rev. B* **91**, 155103 (2015).
  - [21] A. P. Mackenzie, T. Scaffidi, C. W. Hicks, and Y. Maeno, Even odder after twenty-three years: the superconducting order parameter puzzle of  $\text{Sr}_2\text{RuO}_4$ , *npj Quantum Mater.* **2**, 40 (2017).
  - [22] J. R. Kirtley, C. Kallin, C. W. Hicks, E.-A. Kim, Y. Liu, K. A. Moler, Y. Maeno, and K. D. Nelson, Upper limit on spontaneous supercurrents in  $\text{Sr}_2\text{RuO}_4$ , *Phys. Rev. B* **76**, 014526 (2007).
  - [23] C. Lupien, W. A. MacFarlane, Cyril Proust, Louis Taillefer, Z. Q. Mao, and Y. Maeno, Ultrasound attenuation in  $\text{Sr}_2\text{RuO}_4$ : An angle-resolved study of the superconducting gap function, *Phys. Rev. Lett.* **86**, 5986–5989 (2001).
  - [24] E. Hassinger, P. Bourgeois-Hope, H. Taniguchi, S. René de Cotret, G. Grissonnanche, M. S. Anwar, Y. Maeno, N. Doiron-Leyraud, and Louis Taillefer, Vertical line nodes in the superconducting gap structure of  $\text{Sr}_2\text{RuO}_4$ , *Phys. Rev. X* **7**, 011032 (2017).
  - [25] S. Kittaka, S. Nakamura, T. Sakakibara, N. Kikugawa, T. Terashima, S. Uji, D. A. Sokolov, A. P. Mackenzie, K. Irie, Y. Tsutsumi, K. Suzuki, and K. Machida, Searching for gap zeros in  $\text{Sr}_2\text{RuO}_4$  via field-angle-dependent specific-heat measurement, *J. Phys. Soc. Jpn.* **87**, 093703 (2018).
  - [26] S. Kittaka, A. Kasahara, T. Sakakibara, D. Shibata, S. Yonezawa, Y. Maeno, K. Tenya, and K. Machida, Sharp magnetization jump at the first-order superconducting transition in  $\text{Sr}_2\text{RuO}_4$ , *Phys. Rev. B* **90**, 220502 (2014).

- (2014).
- [27] C. W. Hicks, D. O. Brodsky, E. A. Yelland, A. S. Gibbs, J. A. N. Bruin, M. E. Barber, S. D. Edkins, K. Nishimura, S. Yonezawa, Y. Maeno, and A. P. Mackenzie, Strong increase of  $T_c$  of  $\text{Sr}_2\text{RuO}_4$  under both tensile and compressive strain, *Science* **344**, 283–285 (2014).
  - [28] A. Steppke, L. Zhao, M. E. Barber, T. Scaffidi, F. Jerzembeck, H. Rosner, A. S. Gibbs, Y. Maeno, S. H. Simon, A. P. Mackenzie, and C. W. Hicks, Strong peak in  $T_c$  of  $\text{Sr}_2\text{RuO}_4$  under uniaxial pressure, *Science* **355**, eaaf9398 (2017).
  - [29] C. Kallin and A. J. Berlinsky, Is  $\text{Sr}_2\text{RuO}_4$  a chiral  $p$ -wave superconductor? *J. Phys.: Condens. Matter* **21**, 164210 (2009).
  - [30] S. B. Etter, A. Bouhon, and M. Sigrist, Spontaneous surface flux pattern in chiral  $p$ -wave superconductors, *Phys. Rev. B* **97**, 064510 (2018).
  - [31] A. Pustogow, Y. Luo, A. Chronister, Y.-S. Su, D. A. Sokolov, F. Jerzembeck, A. P. Mackenzie, C. W. Hicks, N. Kikugawa, S. Raghu, E. D. Bauer, and S. E. Brown, Constraints on the superconducting order parameter in  $\text{Sr}_2\text{RuO}_4$  from oxygen-17 nuclear magnetic resonance, *Nature (London)* **574**, 72–75 (2019).
  - [32] K. Ishida, M. Manago, K. Kinjo, and Y. Maeno, Reduction of the  $^{17}\text{O}$  Knight shift in the superconducting state and the heat-up effect by NMR pulses on  $\text{Sr}_2\text{RuO}_4$ , *J. Phys. Soc. Jpn.* **89**, 034712 (2020).
  - [33] V. Grinenko, S. Ghosh, R. Sarkar, J.-C. Orain, A. Nikitin, M. Elender, D. Das, Z. Guguchia, F. Brückner, M. E. Barber, J. Park, N. Kikugawa, D. A. Sokolov, J. S. Bobowski, T. Miyoshi, Y. Maeno, A. P. Mackenzie, H. Luetkens, C. W. Hicks, and H.-H. Klauss, Split superconducting and time-reversal symmetry-breaking transitions, and magnetic order in  $\text{Sr}_2\text{RuO}_4$  under uniaxial stress, (2020), arXiv:2001.08152 [cond-mat.supr-con].
  - [34] S. Benhabib, C. Lupien, I. Paul, L. Berges, M. Dion, M. Nardone, A. Zitouni, Z. Q. Mao, Y. Maeno, A. Georges, L. Taillefer, and C. Proust, Jump in the  $c_{66}$  shear modulus at the superconducting transition of  $\text{Sr}_2\text{RuO}_4$ : Evidence for a two-component order parameter, (2020), arXiv:2002.05916 [cond-mat.supr-con].
  - [35] S. Ghosh, A. Shekhter, F. Jerzembeck, N. Kikugawa, D. A. Sokolov, M. Brando, A. P. Mackenzie, C. W. Hicks, and B. J. Ramshaw, Thermodynamic evidence for a two-component superconducting order parameter in  $\text{Sr}_2\text{RuO}_4$ , (2020), arXiv:2002.06130 [cond-mat.supr-con].
  - [36] M. Sigrist and K. Ueda, Phenomenological theory of unconventional superconductivity, *Rev. Mod. Phys.* **63**, 239–311 (1991).
  - [37] I. I. Mazin, Intercalant-driven superconductivity in  $\text{YbC}_6$  and  $\text{CaC}_6$ , *Phys. Rev. Lett.* **95**, 227001 (2005).
  - [38] I. Schnell, I. I. Mazin, and Amy Y. Liu, Unconventional superconducting pairing symmetry induced by phonons, *Phys. Rev. B* **74**, 184503 (2006).
  - [39] H. S. Røising, T. Scaffidi, F. Flicker, G. F. Lange, and S. H. Simon, Superconducting order of  $\text{Sr}_2\text{RuO}_4$  from a three-dimensional microscopic model, *Phys. Rev. Research* **1**, 033108 (2019).
  - [40] C. M. Puetter and H.-Y. Kee, Identifying spin-triplet pairing in spin-orbit coupled multi-band superconductors, *Europhys. Lett.* **98**, 27010 (2012).
  - [41] J. Spałek, Spin-triplet superconducting pairing due to local Hund’s rule and Dirac exchange, *Phys. Rev. B* **63**, 104513 (2001).
  - [42] J. E. Han, Spin-triplet  $s$ -wave local pairing induced by Hund’s rule coupling, *Phys. Rev. B* **70**, 054513 (2004).
  - [43] O. Vafek and A. V. Chubukov, Hund interaction, spin-orbit coupling, and the mechanism of superconductivity in strongly hole-doped iron pnictides, *Phys. Rev. Lett.* **118**, 087003 (2017).
  - [44] A. K. C. Cheung and D. F. Agterberg, Superconductivity in the presence of spin-orbit interactions stabilized by Hund coupling, *Phys. Rev. B* **99**, 024516 (2019).
  - [45] A. W. Lindquist and H.-Y. Kee, Distinct reduction of Knight shift in superconducting state of  $\text{Sr}_2\text{RuO}_4$  under uniaxial strain, (2019), arXiv:1912.02215 [cond-mat.supr-con].
  - [46] S. Hoshino and P. Werner, Superconductivity from emerging magnetic moments, *Phys. Rev. Lett.* **115**, 247001 (2015).
  - [47] O. Gingras, R. Nourafkan, A.-M. S. Tremblay, and M. Côté, Superconducting symmetries of  $\text{Sr}_2\text{RuO}_4$  from first-principles electronic structure, *Phys. Rev. Lett.* **123**, 217005 (2019).
  - [48] A. Tamai, M. Zingl, E. Rozbicki, E. Cappelli, S. Riccò, A. de la Torre, S. McKeown Walker, F. Y. Bruno, P. D. C. King, W. Meevasana, M. Shi, M. Radović, N. C. Plumb, A. S. Gibbs, A. P. Mackenzie, C. Berthod, H. U. R. Strand, M. Kim, A. Georges, and F. Baumberger, High-resolution photoemission on  $\text{Sr}_2\text{RuO}_4$  reveals correlation-enhanced effective spin-orbit coupling and dominantly local self-energies, *Phys. Rev. X* **9**, 021048 (2019).
  - [49] L. Fu and E. Berg, Odd-parity topological superconductors: Theory and application to  $\text{Cu}_x\text{Bi}_2\text{Se}_3$ , *Phys. Rev. Lett.* **105**, 097001 (2010).
  - [50] S. Sasaki, M. Kriener, K. Segawa, K. Yada, Y. Tanaka, M. Sato, and Y. Ando, Topological superconductivity in  $\text{Cu}_x\text{Bi}_2\text{Se}_3$ , *Phys. Rev. Lett.* **107**, 217001 (2011).
  - [51] A. Yamakage, K. Yada, M. Sato, and Y. Tanaka, Theory of tunneling conductance and surface-state transition in superconducting topological insulators, *Phys. Rev. B* **85**, 180509 (2012).
  - [52] A. Ramires and M. Sigrist, Identifying detrimental effects for multiorbital superconductivity: Application to  $\text{Sr}_2\text{RuO}_4$ , *Phys. Rev. B* **94**, 104501 (2016).
  - [53] A. Ramires, D. F. Agterberg, and M. Sigrist, Tailoring  $T_c$  by symmetry principles: The concept of superconducting fitness, *Phys. Rev. B* **98**, 024501 (2018).
  - [54] D. F. Agterberg, P. M. R. Brydon, and C. Timm, Bogoliubov Fermi surfaces in superconductors with broken time-reversal symmetry, *Phys. Rev. Lett.* **118**, 127001 (2017).
  - [55] P. M. R. Brydon, D. F. Agterberg, H. Menke, and C. Timm, Bogoliubov Fermi surfaces: General theory, magnetic order, and topology, *Phys. Rev. B* **98**, 224509 (2018).
  - [56] A. Ramires and M. Sigrist, Superconducting order parameter of  $\text{Sr}_2\text{RuO}_4$ : A microscopic perspective, *Phys. Rev. B* **100**, 104501 (2019).
  - [57] C. N. Veenstra, Z.-H. Zhu, M. Raichle, B. M. Ludbrook, A. Nicolaou, B. Slomski, G. Landolt, S. Kittaka, Y. Maeno, J. H. Dil, I. S. Elfimov, M. W. Haverkort, and A. Damascelli, Spin-orbital entanglement and the breakdown of singlets and triplets in  $\text{Sr}_2\text{RuO}_4$  revealed by spin- and angle-resolved photoemission spectroscopy, *Phys. Rev. Lett.* **112**, 127002 (2014).
  - [58] See Supplemental Material at <http://link.aps.org/supplemental/10.1103/PhysRevResearch.2.032023> for de-

- tails on the construction of the tight-binding model, the linearized gap equation, and the fitness analysis. This includes citations [59–61].
- [59] M. Gradhand, K. I. Wysokinski, J. F. Annett, and B. L. Györfy, Kerr rotation in the unconventional superconductor  $\text{Sr}_2\text{RuO}_4$ , *Phys. Rev. B* **88**, 094504 (2013).
  - [60] W. Huang and H. Yao, Possible three-dimensional nematic odd-parity superconductivity in  $\text{Sr}_2\text{RuO}_4$ , *Phys. Rev. Lett.* **121**, 157002 (2018).
  - [61] D. E. King, Dlib-ml: A machine learning toolkit, *Journal of Machine Learning Research* **10**, 1755–1758 (2009).
  - [62] G. Zhang, E. Gorelov, E. Sarvestani, and E. Pavarini, Fermi surface of  $\text{Sr}_2\text{RuO}_4$ : Spin-orbit and anisotropic coulomb interaction effects, *Phys. Rev. Lett.* **116**, 106402 (2016).
  - [63] E. Dagotto, T. Hotta, and A. Moreo, Colossal magnetoresistant materials: The key role of phase separation, *Physics Reports* **344**, 1–153 (2001).
  - [64] D. F. Agterberg, T. M. Rice, and M. Sgrist, Orbital dependent superconductivity in  $\text{Sr}_2\text{RuO}_4$ , *Phys. Rev. Lett.* **78**, 3374–3377 (1997).
  - [65] Y. Yu, A. K. C. Cheung, S. Raghu, and D. F. Agterberg, Residual spin susceptibility in the spin-triplet orbital-singlet model, *Phys. Rev. B* **98**, 184507 (2018).
  - [66] S. Kashiwaya, K. Saitoh, H. Kashiwaya, M. Koyanagi, M. Sato, K. Yada, Y. Tanaka, and Y. Maeno, Time-reversal invariant superconductivity of  $\text{Sr}_2\text{RuO}_4$  revealed by Josephson effects, *Phys. Rev. B* **100**, 094530 (2019).
  - [67] C. J. Lapp, G. Börner, and C. Timm, Experimental consequences of Bogoliubov Fermi surfaces, *Phys. Rev. B* **101**, 024505 (2020).
  - [68] R. Sharma, S. D. Edkins, Z. Wang, A. Kostin, C. Sow, Y. Maeno, A. P. Mackenzie, J. C. Séamus Davis, and V. Madhavan, Momentum-resolved superconducting energy gaps of  $\text{Sr}_2\text{RuO}_4$  from quasiparticle interference imaging, *Proc. Natl. Acad. Sci. USA* **117**, 5222–5227 (2020).



# Supplemental Material for Stabilizing Even-Parity Chiral Superconductivity in $\text{Sr}_2\text{RuO}_4$

Han Gyeol Suh, Henri Menke, P. M. R. Brydon, Carsten Timm, Aline Ramires, and Daniel F. Agterberg

## MICROSCOPIC MODEL

In this section, we construct a 3D tight-binding model for  $\text{Sr}_2\text{RuO}_4$ . We take into account the full 3D Fermi surfaces (FSs) of  $\text{Sr}_2\text{RuO}_4$ , based on the DFT band structure obtained by Veenstra *et al.* [1], who showed that despite the 2D shape of the FSs, the orbital and spin polarization vary along  $k_z$ . To account for the presence of orbital mixing on the different FS sheets, we include the  $t_{2g}$  manifold of the Ru  $d_{yz}$ ,  $d_{xz}$ , and  $d_{xy}$  orbitals (we will assume this order throughout).

We parametrize the orbital space by the Gell-Mann matrices, which are the generators of  $\text{SU}(3)$ . We use the convention

$$\begin{aligned} \lambda_0 &= \begin{pmatrix} 1 & 0 & 0 \\ 0 & 1 & 0 \\ 0 & 0 & 1 \end{pmatrix}, \quad \lambda_1 = \begin{pmatrix} 0 & 1 & 0 \\ 1 & 0 & 0 \\ 0 & 0 & 0 \end{pmatrix}, \quad \lambda_2 = \begin{pmatrix} 0 & 0 & 1 \\ 0 & 0 & 0 \\ 1 & 0 & 0 \end{pmatrix}, \quad \lambda_3 = \begin{pmatrix} 0 & 0 & 0 \\ 0 & 0 & 1 \\ 0 & 1 & 0 \end{pmatrix}, \quad \lambda_4 = \begin{pmatrix} 0 & -i & 0 \\ i & 0 & 0 \\ 0 & 0 & 0 \end{pmatrix}, \\ \lambda_5 &= \begin{pmatrix} 0 & 0 & -i \\ 0 & 0 & 0 \\ i & 0 & 0 \end{pmatrix}, \quad \lambda_6 = \begin{pmatrix} 0 & 0 & 0 \\ 0 & 0 & -i \\ 0 & i & 0 \end{pmatrix}, \quad \lambda_7 = \begin{pmatrix} 1 & 0 & 0 \\ 0 & -1 & 0 \\ 0 & 0 & 0 \end{pmatrix}, \quad \lambda_8 = \frac{1}{\sqrt{3}} \begin{pmatrix} 1 & 0 & 0 \\ 0 & 1 & 0 \\ 0 & 0 & -2 \end{pmatrix}. \end{aligned} \quad (\text{S1})$$

We write the normal-state Hamiltonian in terms of the spinor  $\Phi_{\mathbf{k}} = (c_{\mathbf{k},2,\uparrow}, c_{\mathbf{k},2,\downarrow}, c_{\mathbf{k},1,\uparrow}, c_{\mathbf{k},1,\downarrow}, c_{\mathbf{k},3,\uparrow}, c_{\mathbf{k},3,\downarrow})^T$ , where we introduce the numbering of the orbitals  $1 = d_{xz}$ ,  $2 = d_{yz}$ ,  $3 = d_{xy}$ . In terms of the Gell-Mann and Pauli matrices, we write the Hamiltonian  $H_0 = \sum_{\mathbf{k}} \Phi_{\mathbf{k}}^\dagger \hat{H}_0(\mathbf{k}) \Phi_{\mathbf{k}}$  where

$$\hat{H}_0(\mathbf{k}) = \sum_{a,b} h_{ab}(\mathbf{k}) \lambda_a \otimes \sigma_b. \quad (\text{S2})$$

In the presence of inversion and time-reversal symmetries, only a subset of fifteen  $h_{ab}(\mathbf{k})$  terms are allowed. Table S1 lists the symmetry-allowed terms, the associated irrep for the matrices  $\lambda_a \otimes \sigma_b$ , the physical process to which these correspond, and their momentum dependence.

Irrep	(a, b)	Type	Explicit form of $h_{ab}(\mathbf{k})$
$A_{1g}$	(0, 0)	intra-orbital hopping	$\frac{1}{3} [\xi_{11}(\mathbf{k}) + \xi_{22}(\mathbf{k}) + \xi_{33}(\mathbf{k})]$
	(8, 0)	intra-orbital hopping	$\frac{1}{2\sqrt{3}} [\xi_{11}(\mathbf{k}) + \xi_{22}(\mathbf{k}) - 2\xi_{33}(\mathbf{k})]$
	(4, 3)	atomic SOC	$-\eta_z$
	(5, 2) - (6, 1)	atomic-SOC	$\eta_\perp$
$A_{2g}$	(5, 1) + (6, 2)	$\mathbf{k}$ -SOC	neglected
$B_{1g}$	(7, 0)	intra-orbital hopping	$\frac{1}{2} [\xi_{22}(\mathbf{k}) - \xi_{11}(\mathbf{k})]$
	(5, 2) + (6, 1)	$\mathbf{k}$ -SOC	$2t_{5261}^{\text{SOC}} (\cos k_x a - \cos k_y a)$
$B_{2g}$	(1, 0)	inter-orbital hopping	$\lambda(\mathbf{k})$
	(5, 1) - (6, 2)	$\mathbf{k}$ -SOC	$4t_{5162}^{\text{SOC}} \sin k_x a \sin k_y a$
$E_g$	{(2, 0), (3, 0)}	inter-orbital hopping	$8t_z^{13} \sin(k_z c/2) \{\sin(k_x a/2) \cos(k_y a/2), \cos(k_x a/2) \sin(k_y a/2)\}$
	{(4, 1), (4, 2)}	$\mathbf{k}$ -SOC	$8t_{12z}^{\text{SOC}} \sin(k_z c/2) \{\sin(k_x a/2) \cos(k_y a/2), \cos(k_x a/2) \sin(k_y a/2)\}$
	{(6, 3), -(5, 3)}	$\mathbf{k}$ -SOC	$-8t_{56z}^{\text{SOC}} \sin(k_z c/2) \{\sin(k_x a/2) \cos(k_y a/2), \cos(k_x a/2) \sin(k_y a/2)\}$

TABLE S1. List of the fifteen symmetry-allowed terms in the normal-state Hamiltonian  $\hat{H}_0(\mathbf{k})$  in Eq. (S2). For each (a, b), the basis function  $h_{ab}(\mathbf{k})$  must belong to the same irrep of  $D_{4h}$  as the matrix  $\lambda_a \otimes \sigma_b$ . The table gives the irrep, the associated physical process (“Type”), where “ $\mathbf{k}$ -SOC” means momentum-dependent (nonlocal) SOC, and the momentum dependence of  $h_{ab}(\mathbf{k})$ . For the two-dimensional irrep  $E_g$ , the entries are organized such that the first transforms as  $xz$  and the second as  $yz$ .



Note that Table S1 has entries which are in accordance with previous literature [2–4] but there are also new terms associated with hopping along the  $z$ -direction or momentum-dependent SOC, which are usually neglected. Here we take  $\eta_z = \eta_\perp = \eta$  as the parameter for the on-site atomic SOC. The intra-orbital hoppings  $\xi_{11,22,33}(\mathbf{k})$  are included up to next-next-nearest neighbors in plane and next-nearest neighbors out of plane. The inter-orbital hopping  $\lambda(\mathbf{k})$  between the  $d_{xz}$  and the  $d_{yz}$  orbitals is kept up to next-nearest neighbors in plane and nearest neighbors out of plane. For the inter-orbital hopping  $\{(3,0), -(2,0)\}$  between the  $d_{xz}$  and  $d_{xy}$  ( $d_{yz}$  and  $d_{xy}$ ) orbitals, we only keep the nearest-neighbor component out of plane. The explicit form of the functions not given explicitly in Table S1 is

$$\begin{aligned}\xi_{11,22}(\mathbf{k}) = & 2t_{x,y}^{11} \cos k_x a + 2t_{y,x}^{11} \cos k_y a \\ & + 8t_z^{11} \cos(k_x a/2) \cos(k_y a/2) \cos(k_z c/2) \\ & + 4t_{xy}^{11} \cos k_x a \cos k_y a + 2t_{xx,yy}^{11} \cos 2k_x a + 2t_{yy,xx}^{11} \cos 2k_y a \\ & + 4t_{xxy,xyy}^{11} \cos 2k_x a \cos k_y a + 4t_{xyy,xyx}^{11} \cos 2k_y a \cos k_x a \\ & + 2t_{zz}^{11} (\cos k_z c - 1) - \mu, \end{aligned} \quad (\text{S3})$$

$$\begin{aligned}\xi_{33}(\mathbf{k}) = & 2t_x^{33} (\cos k_x a + \cos k_y a) \\ & + 8t_z^{33} \cos(k_x a/2) \cos(k_y a/2) \cos(k_z c/2) \\ & + 4t_{xy}^{33} \cos k_x a \cos k_y a + 2t_{xx}^{33} (\cos 2k_x a + \cos 2k_y a) \\ & + 4t_{xxy}^{33} (\cos 2k_x a \cos k_y a + \cos 2k_y a \cos k_x a) \\ & + 2t_{zz}^{33} (\cos k_z c - 1) - \mu_1, \end{aligned} \quad (\text{S4})$$

$$\begin{aligned}\lambda(\mathbf{k}) = & 4t_z^{12} \sin(k_x a/2) \sin(k_y a/2) \cos(k_z c/2) \\ & - 4t_{xy}^{12} \sin k_x a \sin k_y a \\ & - 4t_{xxy}^{12} (\sin 2k_x a \sin k_y a + \sin 2k_y a \sin k_x a). \end{aligned} \quad (\text{S5})$$

We now focus on terms corresponding to  $\mathbf{k}$ -dependent SOC, usually not taken into account in the standard parametrization of the normal-state Hamiltonian. The first matrix in the list,  $\lambda_5 \otimes \sigma_1 + \lambda_6 \otimes \sigma_2$ , which is of  $A_{2g}$  symmetry, will be ignored because the lowest-order polynomial basis function of this irrep is of order 4 ( $g$ -wave), which only appears at next-next-next-nearest-neighbor hopping and is therefore assumed to be negligible. We also take the other  $\mathbf{k}$ -dependent SOC terms at the lowest order at which they appear. This concludes the construction of the microscopic model, which is characterized by a Hamiltonian with 26 free parameters.

## FIT TO DFT RESULTS

We employ the tight-binding model presented in the supplemental material of [1] to determine the free parameters. The tight-binding Hamiltonian is derived from an LDA band structure that is down-folded onto the O-2p and the Ru-4d orbitals and therefore has a total of 17 bands. The hopping integrals are truncated at 10 meV. We henceforth refer to the LDA-derived tight-binding Hamiltonian as the “DFT model”. For the calculation of the linearized gap equation, the DFT model is much too large and most of the bands are irrelevant for superconductivity. The states at the Fermi surface are determined by the  $t_{2g}$  manifold of the Ru-4d orbitals ( $d_{yz}$ ,  $d_{xz}$ ,  $d_{xy}$ ) and we fit Eq. (S2) to several quantities extracted from the DFT model projected into this subspace.

We extract the Fermi momenta  $\tilde{\mathbf{k}}_F$  of the DFT model and denote the eigenvalues by  $\epsilon$  and the associated eigenvectors by  $V$ . We define the following measure

$$S = \sum_{n=\alpha,\beta,\gamma, \tilde{\mathbf{k}}_F} \left[ (\epsilon^n(\tilde{\mathbf{k}}_F))^2 + (\tilde{d}_{xy}^n(\tilde{\mathbf{k}}_F) - d_{xy}^n(\tilde{\mathbf{k}}_F))^2 + (\tilde{p}_{\text{SOC}}^n(\tilde{\mathbf{k}}_F) - p_{\text{SOC}}^n(\tilde{\mathbf{k}}_F))^2 + (\tilde{v}_{\parallel}^n(\tilde{\mathbf{k}}_F) - v_{\parallel}^n(\tilde{\mathbf{k}}_F))^2 \right], \quad (\text{S6})$$

where the sum is over momenta  $\tilde{\mathbf{k}}_F$  on the DFT Fermi surfaces formed by the bands  $n = \alpha, \beta, \gamma$ ,  $\epsilon^n(\mathbf{k})$  are the band energies,  $d_{xy}^n(\mathbf{k})$  is the  $d_{xy}$ -orbital content,  $p_{\text{SOC}}^n(\mathbf{k})$  is the spin polarization, and  $v_{\parallel}^n(\mathbf{k})$  the in-plane velocity. Quantities with a tilde are from the DFT model. The  $d_{xy}$ -orbital content is determined by the corresponding eigenvector components

$$d_{xy}^n(\mathbf{k}) = \frac{1}{2} (|V_{d_{xy},\uparrow}^{n,\uparrow}(\mathbf{k})|^2 + |V_{d_{xy},\downarrow}^{n,\uparrow}(\mathbf{k})|^2 + |V_{d_{xy},\uparrow}^{n,\downarrow}(\mathbf{k})|^2 + |V_{d_{xy},\downarrow}^{n,\downarrow}(\mathbf{k})|^2). \quad (\text{S7})$$

$t_x^{11}$	-362.4	$t_y^{11}$	-134	$t_x^{33}$	-262.4	$t_{xy}^{11}$	-44.01	$t_{xx}^{11}$	-1.021
$t_{yy}^{11}$	-5.727	$t_{xy}^{33}$	-43.73	$t_{xx}^{33}$	34.23	$t_{xy}^{12}$	16.25	$t_{xxy}^{11}$	-13.93
$t_{xyy}^{11}$	-7.52	$t_{xxy}^{33}$	8.069	$t_{xxy}^{12}$	3.94	$\eta$	57.39	$\mu$	438.5
$\mu_1$	218.6	$t_z^{11}$	-0.0228	$t_z^{33}$	1.811	$t_z^{12}$	19.95	$t_z^{13}$	8.304
$t_{zz}^{11}$	2.522	$t_{zz}^{33}$	-3.159	$t_{56z}^{\text{SOC}}$	-1.247	$t_{12z}^{\text{SOC}}$	-3.576	$t_{5162}^{\text{SOC}}$	-1.008
$t_{5261}^{\text{SOC}}$	0.3779								

TABLE S2. Parameters of the Hamiltonian (S2) determined from the fit to the DFT model. All values are in meV.

The spin polarization is determined from the expectation value of the atomic spin-orbit coupling Hamiltonian  $H_{\text{SOC}} = \lambda_5 \sigma_2 - \lambda_6 \sigma_1 - \lambda_4 \sigma_3$ :

$$p_{\text{SOC}}^n(\mathbf{k}) = 1 + \left[ \frac{1}{2} \text{Re}(V^{n,\uparrow T}(\mathbf{k}) H_{\text{SOC}} V^{n,\uparrow}(\mathbf{k}) + V^{n,\downarrow T}(\mathbf{k}) H_{\text{SOC}} V^{n,\downarrow}(\mathbf{k})) \right]^{1/3}. \quad (\text{S8})$$

For the in-plane Fermi velocity we use a simple two-point central finite differences stencil where  $\varepsilon_{x,y}$  are small

$$v_{\parallel}^n(\mathbf{k}) = \sqrt{\left| \frac{\epsilon^n(\mathbf{k} - \varepsilon_x) - \epsilon^n(\mathbf{k} + \varepsilon_x)}{2\varepsilon_x} \right|^2 + \left| \frac{\epsilon^n(\mathbf{k} - \varepsilon_y) - \epsilon^n(\mathbf{k} + \varepsilon_y)}{2\varepsilon_y} \right|^2}. \quad (\text{S9})$$

We minimize the measure (S6) using the derivative-free optimization algorithm BOBYQA of dlib [5].

The fit yields very good agreement with the DFT model close to the Fermi energy, including good reproduction of the  $d_{xy}$ -orbital content and the spin polarization. In Fig. S1, we compare the result of our fit with the DFT model in the  $k_z = 0$  plane. In Fig. S2, we show the full 3D Fermi surface produced by our fit, together with the  $d_{xy}$ -orbital content and the spin polarization. The corresponding fit parameters are listed in Tab. S2.

It is important to note that because the different sheets of the Fermi surface have varying orbital and spin content, it is not possible to isolate one dominant band for superconductivity. The pairing state will in general have contributions from all three sheets.

## LINEARIZED GAP EQUATION

In this section, we outline our solution of the linearized BCS gap equation. For convenience, we repeat the second-order expansion of the free energy as given in Eq. (3) of the main text,

$$\mathcal{F} = \frac{1}{2} \sum_i \frac{1}{g_i} \text{Tr} [\hat{\Delta}_i^\dagger \hat{\Delta}_i] - \frac{k_B T}{2} \sum_{\mathbf{k}, \omega, i, j} \text{Tr} [\hat{\Delta}_i \hat{G} \hat{\Delta}_j^\dagger \hat{G}], \quad (\text{S10})$$

where the gap functions are  $\hat{\Delta}_i = \Delta_i \lambda_{a_i} \otimes \sigma_{b_i} (i\sigma_2)$  and the indices  $a_i$ ,  $b_i$ , and interaction energies  $g_i$  are given in Table 1 of the main text. We introduce an interaction scaling parameter  $s$ , and for concreteness choose the interaction energies to be given by  $U = 5/s$ ,  $U' = 1/s$ , and  $J = 2/s$ . Since we are interested in the weak-coupling limit we will later assume  $s$  to be large. The Green's functions and gap function are expressed in the energy eigenbasis by

$$\hat{G} \rightarrow U^\dagger \hat{G} U = \text{diag} \left( \frac{1}{i\omega_n - \epsilon_a} \right), \quad (\text{S11})$$

$$\underline{\hat{G}} \rightarrow \underline{U}^\dagger \underline{\hat{G}} \underline{U} = \text{diag} \left( \frac{1}{i\omega_n + \epsilon_a} \right), \quad (\text{S12})$$

$$\hat{\Delta}_i \rightarrow U^\dagger \hat{\Delta}_i U, \quad (\text{S13})$$

where  $U$  is a unitary matrix that diagonalizes the normal-state Hamiltonian  $\hat{H}_0$ ,  $\underline{U} = (i\sigma_2)^\dagger U$ , and  $\epsilon_a$  are band energies. We define new gap matrices by

$$\Lambda_i = U^\dagger (\lambda_{a_i} \otimes \sigma_{b_i}) U. \quad (\text{S14})$$

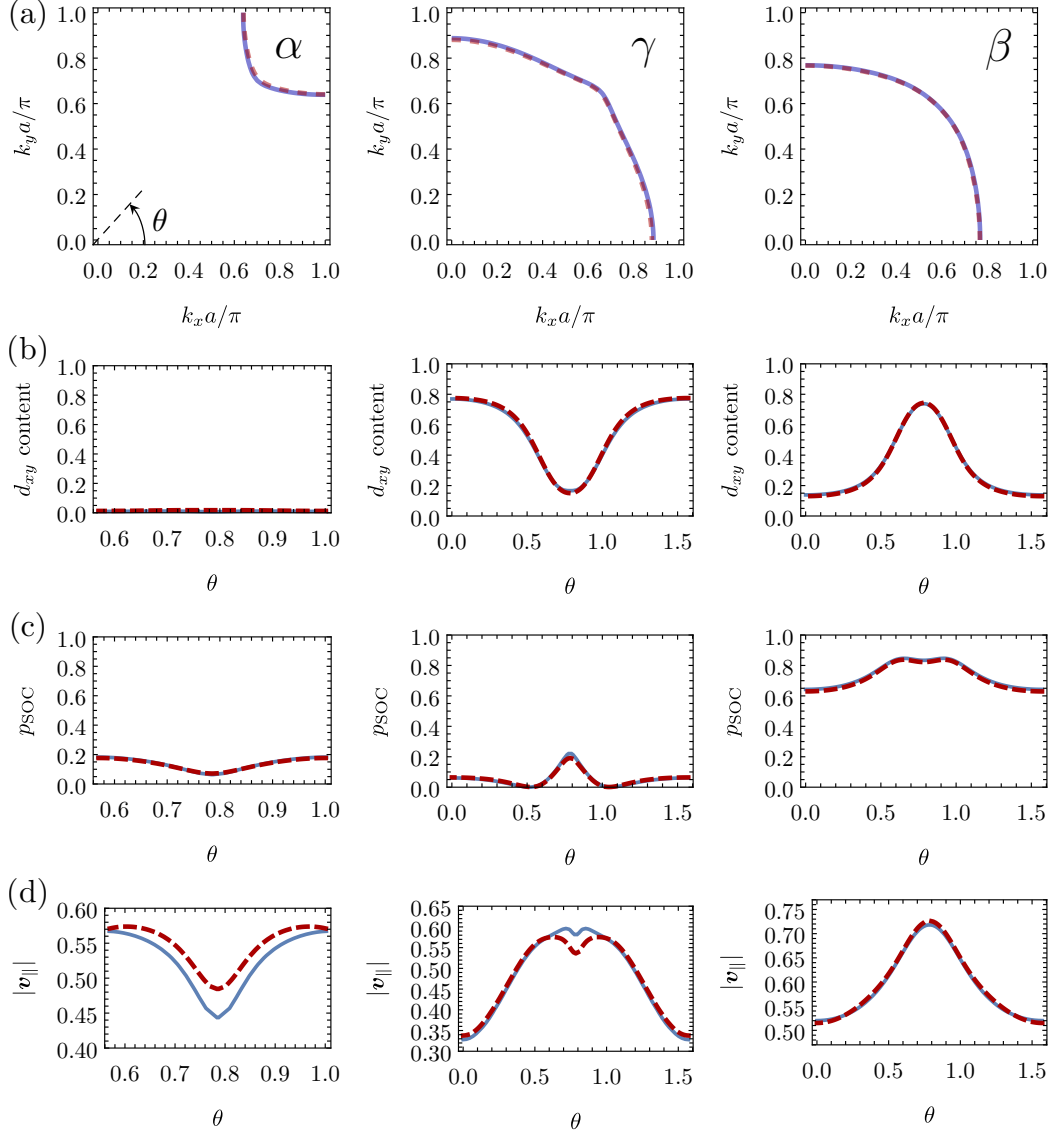


FIG. S1. Comparison of the DFT model (red dashed lines) with our fit (blue solid lines) in the  $k_z = 0$  plane. (a) Fermi surface in the first quadrant of the Brillouin zone. (b)  $d_{xy}$ -orbital content, (c) spin polarization, and (d) in-plane velocity as functions of the angle  $\theta = \arctan(k_y/k_x)$  in the first quadrant. The three columns pertain to the  $\alpha$ ,  $\gamma$ , and  $\beta$  band.

The frequency summation yields

$$S_{ab}(\mathbf{k}, \beta) = -\frac{1}{\beta} \sum_{\omega_n} \frac{1}{i\omega_n - \epsilon_a} \frac{1}{i\omega_n + \epsilon_b} = \frac{1}{2} \frac{\tanh(\beta\epsilon_a/2) + \tanh(\beta\epsilon_b/2)}{\epsilon_a + \epsilon_b}, \quad (\text{S15})$$

where  $\beta = 1/k_B T$ . The linearized gap equations are obtained by differentiating the free energy with respect to the gap amplitudes,  $\partial\mathcal{F}/\partial\Delta_i^* = 0$ , written explicitly as

$$\sum_j \left( s \frac{\delta_{ij}}{\tilde{g}_i} \text{Tr} [\Lambda_i^\dagger \Lambda_i] + \sum_{\mathbf{k}, a, b} [\Lambda_i]_{ab}^* [\Lambda_j]_{ab} S_{ab} \right) \Delta_j = 0, \quad (\text{S16})$$

where  $i$  and  $j$  run over all gap-structure indices of a given irrep,  $a$  and  $b$  run over band indices,  $[\Lambda_i]_{ab}$  is a matrix element of  $\Lambda_i$ , and  $\tilde{g}_i$  is the value of  $g_i$  when  $s = 1$ .

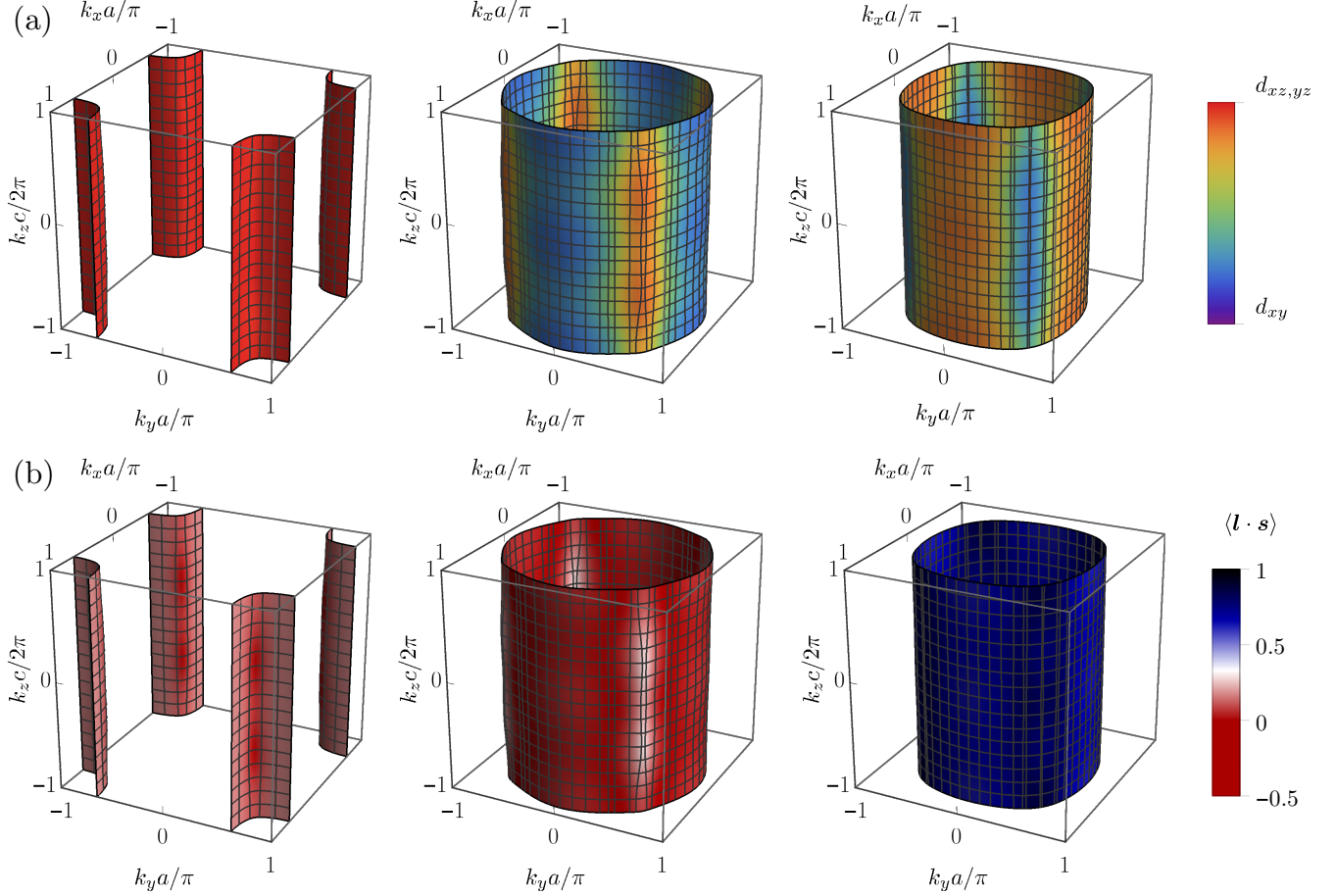


FIG. S2. Full 3D Fermi surface obtained from the best fit to the DFT results of Ref. [1], with color indicating (a) the  $d_{xy}$ -orbital content and (b) the spin polarization. The three columns pertain to the  $\alpha$ ,  $\gamma$ , and  $\beta$  band.

First, consider  $\epsilon_a = \epsilon_b$  intraband terms in Eq. (S16), the  $\mathbf{k}$ -integration is written as

$$\sum_{\mathbf{k}, \epsilon_a = \epsilon_b} [\Lambda_i]_{ab}^* [\Lambda_j]_{ab} S_{ab} = \sum_{\epsilon_a = \epsilon_b} \frac{1}{2} \int d\epsilon F_{abij}(\epsilon) \frac{\tanh(\beta\epsilon/2)}{\epsilon}, \quad (\text{S17})$$

with

$$F_{abij}(\epsilon) = \frac{1}{(2\pi)^3} \iint_{\epsilon_a(\mathbf{k}) = \epsilon} d^2\mathbf{k} \frac{\delta_{\epsilon_a \epsilon_b}}{\|\nabla \epsilon_a\|} [\Lambda_i]_{ab}^* [\Lambda_j]_{ab}. \quad (\text{S18})$$

Use the Taylor expansion of  $F_{abij}(\epsilon)$  around the Fermi level,  $F_{abij}(0) + \epsilon F'_{abij}(0) + \dots$ , the derivative of Eq. (S17) with respect to  $\beta$  gives

$$\frac{\partial}{\partial \beta} \sum_{\mathbf{k}, \epsilon_a = \epsilon_b} [\Lambda_i]_{ab}^* [\Lambda_j]_{ab} S_{ab} = \frac{1}{\beta} \sum_{\epsilon_a = \epsilon_b} F_{abij}(0) + O\left(\frac{1}{\beta^3}\right). \quad (\text{S19})$$

Note that when this is integrated with respect to  $\beta$  it yields the  $\log \beta$  divergence in Eq. (S17). Next, consider the  $\epsilon_a \neq \epsilon_b$  interband terms, as  $\beta \rightarrow \infty$ ,  $S_{ab}$  converges to  $\theta(\epsilon_a \epsilon_b)/|\epsilon_a + \epsilon_b|$ , where  $\theta$  is the Heaviside step function. Because this is a bounded function, there is no divergence in the interband contributions. In Eq. (S16) a non-trivial solution for the gap amplitudes  $\Delta_j$  is found by considering  $i$  and  $j$  as matrix indices and taking the corresponding  $6 \times 6$  matrix to be singular. Including both the intraband and interband contributions, the critical  $\beta_c$  satisfies

$$\det \left[ s \frac{\delta_{ij}}{\tilde{g}_i} \text{Tr} [\Lambda_i^\dagger \Lambda_i] + \log \beta_c \sum_{\epsilon_a = \epsilon_b} F_{abij}(0) + C_{ij}(\beta_c) \right] = 0, \quad (\text{S20})$$

where  $C_{ij}(\beta)$  is the portion of  $\sum_{\mathbf{k}, a, b} [\Lambda_i]_{ab}^* [\Lambda_j]_{ab} S_{ab}$  that remains after removing the  $\log \beta$  divergent term. By definition,  $C_{ij}(\beta)$  is convergent as  $\beta \rightarrow \infty$ , so the last term in the determinant can be ignored when  $s$  is sufficiently large. More explicitly, in the weak-coupling limit  $s \rightarrow \infty$ ,  $T_c$  is given in the form

$$\log T_c(s) \approx -ms + \delta, \quad (\text{S21})$$

where  $\delta$  is a constant and  $m$  is the smallest  $\log \beta_c/s$  solution found when  $C_{ij} = 0$ .

Different channels (irreps) have different values of  $m$ , and the channel with the smallest  $m$  is the leading instability in the weak-coupling limit. Note that the definition of  $m$  does not depend on  $C_{ij}$  and all the interband contributions go into  $C_{ij}$ . Thus we can drop the interband terms in Eq. (S16). This changes  $\delta$  but does not change  $m$ . The resultant expression is

$$\det \left[ s \frac{\delta_{ij}}{g_i} \text{Tr} [\Lambda_i^\dagger \Lambda_i] + \sum_{\mathbf{k}, \epsilon_a = \epsilon_b} [\Lambda_i]_{ab}^* [\Lambda_j]_{ab} S_{ab} \right] = 0, \quad (\text{S22})$$

which is the equation we solve numerically. The  $\log \beta$  divergence originates from momenta near the Fermi surface, so we carry out the  $\mathbf{k}$ -integration on adaptive meshes with finer resolution near the Fermi surface. We obtain  $\log \beta_c$  for several values of  $s$  and use linear regression to get the slope, which determines  $m$ . If the values of  $\log \beta_c$  at the sampling points are not linear in  $s$  we sample larger  $s$  values until we encounter linear behavior. In our calculation, an equidistant set of four sampling points is used for a linear regression and their  $R^2$  measures are always greater than 0.999. Using this procedure, we get the slope  $m$  for each pairing channel and determine the leading instability at each point in the phase diagram displayed in Fig. 1(a) in the main text. While this procedure may seem more elaborate than a direct solution of Eq. (S20) with  $C_{ij} = 0$ , it allows us to verify Eq. (S21) showing that our solution is in the weak coupling limit.

## SUPERCONDUCTING-FITNESS ANALYSIS

In this section, we present details of the superconducting-fitness analysis. We start with the more realistic three-orbital model and then consider an effective two-orbital model, which dramatically simplifies the analysis but gives consistent results.

### Complete 3D three-orbital model

In previous works [6, 7], a proof of the direct relation between the superconducting-fitness measures  $\hat{F}_C(\mathbf{k})$  and  $\hat{F}_A(\mathbf{k})$  (defined below) and the superconducting critical temperature was provided for the one- and two-orbital scenario. The first measure,

$$\hat{F}_C(\mathbf{k}) = \tilde{H}_0(\mathbf{k}) \tilde{\Delta}(\mathbf{k}) - \tilde{\Delta}(\mathbf{k}) \tilde{H}_0^*(-\mathbf{k}), \quad (\text{S23})$$

quantifies how incompatible a given gap structure is for a specific normal state, namely, how much inter-band pairing there is. Here,  $\tilde{H}_0(\mathbf{k}) = \hat{H}_0(\mathbf{k}) - h_{00}(\mathbf{k}) \lambda_0 \otimes \sigma_0$  and we have defined a normalized gap matrix  $\tilde{\Delta}(\mathbf{k}) = \hat{\Delta}(\mathbf{k})/|\hat{\Delta}(\mathbf{k})|$  such that average over the normal-state Fermi surface is  $\langle \tilde{\Delta}(\mathbf{k}) \tilde{\Delta}^\dagger(\mathbf{k}) \rangle_{\text{FS}} = \mathbb{I}$ . The second measure,

$$\hat{F}_A(\mathbf{k}) = \tilde{H}_0(\mathbf{k}) \tilde{\Delta}(\mathbf{k}) + \tilde{\Delta}(\mathbf{k}) \tilde{H}_0^*(-\mathbf{k}), \quad (\text{S24})$$

quantifies how much intra-band pairing there is, or what fraction of the gap survives upon projection onto the Fermi surface. For the two-orbital scenario, these measures satisfy  $\langle \text{Tr} \hat{F}_A^\dagger(\mathbf{k}) \hat{F}_A(\mathbf{k}) + \text{Tr} \hat{F}_C^\dagger(\mathbf{k}) \hat{F}_C(\mathbf{k}) \rangle_{\text{FS}} = 1$ , up to normalization of the normal-state Hamiltonian, which highlights their complementarity. The proof of this relation relies on the fact that the matrices associated with the orbital DOF are Pauli matrices for the two-orbital scenario and therefore form a totally anticommuting set, which greatly simplifies the calculations. On the other hand, for  $n > 2$  orbitals, the basis matrices are the generators of  $\text{SU}(n)$ , which do not form a totally anticommuting set and therefore do not allow a direct generalization of this relation for models with more than two orbitals. However, the physical meaning of  $\hat{F}_C(\mathbf{k})$  and  $\hat{F}_A(\mathbf{k})$  is preserved within some approximations, as discussed below.

For the three-orbital situation, the corresponding superconducting-fitness functions can be identified as

$$\hat{F}_{A,C}^{3orb}(\mathbf{k}) = [\hat{H}_0(\mathbf{k})]^2 \tilde{\Delta}(\mathbf{k}) \pm \tilde{\Delta}(\mathbf{k}) [\hat{H}_0^*(-\mathbf{k})]^2. \quad (\text{S25})$$

Irrep	$[a, b]$	Interac.	$A_{1g}$			$A_{2g}$	$B_{1g}$		$B_{2g}$		$E_g$					
			$h_{80}$	$h_{43}$	$h_{52-61}$	$h_{51+62}$	$h_{70}$	$h_{52+61}$	$h_{10}$	$h_{51-62}$	$h_{20}$	$h_{30}$	$h_{41}$	$h_{42}$	$h_{53}$	$h_{63}$
$A_{1g}$	$[0, 0]$	$U + 2J'$	$\frac{32}{3}$	$\frac{32}{3}$	$\frac{64}{3}$	$\frac{128}{3}$	$\frac{32}{3}$	$\frac{128}{3}$	$\frac{32}{3}$	$\frac{64}{3}$	$\frac{32}{3}$	$\frac{32}{3}$	$\frac{32}{3}$	$\frac{32}{3}$	$\frac{32}{3}$	$\frac{32}{3}$
	$[8, 0]$	$U - J'$	16	$\frac{16}{3}$	$\frac{8}{3}$	$\frac{16}{3}$	$\frac{16}{3}$	$\frac{16}{3}$	$\frac{16}{3}$	$\frac{8}{3}$	$\frac{4}{3}$	$\frac{4}{3}$	$\frac{16}{3}$	$\frac{16}{3}$	$\frac{4}{3}$	$\frac{4}{3}$
	$[4, 3]$	$U' - J$	$\frac{16}{3}$	16	8	16	0	16	0	8	4	4	0	0	4	4
	$[5, 2] - [6, 1]$	$U' - J$	$\frac{5}{3}$	3	24	8	3	8	3	8	2	2	4	4	2	2
$A_{2g}$	$[5, 1] + [6, 2]$	$U' - J$	$\frac{5}{3}$	3	0	32	3	32	3	8	2	2	4	4	2	2
$B_{1g}$	$[7, 0]$	$U - J'$	$\frac{16}{3}$	0	8	16	16	16	0	8	4	4	0	0	4	4
	$[5, 2] + [6, 1]$	$U' - J$	$\frac{5}{3}$	3	8	32	3	32	3	0	2	2	4	4	2	2
$B_{2g}$	$[1, 0]$	$U' + J$	$\frac{16}{3}$	0	8	16	0	16	16	8	4	4	0	0	4	4
	$[5, 1] - [6, 2]$	$U' - J$	$\frac{5}{3}$	3	8	8	3	8	3	24	2	2	4	4	2	2
$E_g$	$+ [3, 0]$	$U' + J$	$\frac{4}{3}$	4	4	8	4	8	4	4	4	16	4	4	4	0
	$- [2, 0]$		$\frac{4}{3}$	4	4	8	4	8	4	4	16	4	4	4	0	4
$E_g$	$+ [4, 2]$	$U' - J$	$\frac{16}{3}$	0	8	16	0	16	0	8	4	4	0	16	4	4
	$- [4, 1]$		$\frac{16}{3}$	0	8	16	0	16	0	8	4	4	16	0	4	4
$E_g$	$+ [5, 3]$	$U' - J$	$\frac{4}{3}$	4	4	8	4	8	4	4	0	4	4	4	16	4
	$+ [6, 3]$		$\frac{4}{3}$	4	4	8	4	8	4	4	4	0	4	4	4	16

TABLE S3. Superconducting-fitness measure  $\hat{F}_A$  for the 3D three-orbital model for  $\text{Sr}_2\text{RuO}_4$ . The first column gives the irreps of the order parameters associated with matrix form  $[a, b]$  (second column) and the third column displays the local interaction in the respective channel, where the potentially attractive channels are highlighted in boldface. Columns 4–17 give the results for the fitness function such that  $\text{Tr } \hat{F}_A^\dagger \hat{F}_A = \sum_{cd} (\text{table entry}) |h_{cd}|^2$ , for each term  $h_{cd}$  in the normal-state Hamiltonian, indicated in the second row with the associated irrep given in the first row. We highlight in boldface the  $h_{cd}$  terms which are present in the standard 2D models for  $\text{Sr}_2\text{RuO}_4$ , while the terms in normal typeface are either momentum-dependent SOC or interlayer couplings.

Given that  $[A^2, B]_\pm = A[A, B] \mp [A, B]A$ , the core of the analysis still depends on the original form of the superconducting-fitness functions. Therefore, we use the form linear in  $\hat{H}_0(\mathbf{k})$  to get some insight. Below, we will see that a simplified two-orbital model, for which the linear version of the fitness functions is valid rigorously, corroborates our analysis. We summarize the results for the complete three-orbital problem in Tables S3 and S4. The first row gives the irrep of each term in the normal-state Hamiltonian displayed in the second row as  $h_{ab}$ . The first column gives the irrep of each order parameter displayed in the second column following the notation  $[a, b]$  corresponding to  $\hat{\Delta} = \lambda_a \otimes \sigma_b (i\sigma_2)$ . The third column gives the interaction stemming from the Hubbard-Kanamori Hamiltonian for each channel. Finally, the numerical entries in the tables correspond to  $\text{Tr } \hat{F}_{A,C}^\dagger \hat{F}_{A,C} = \sum_{cd} (\text{table entry}) |h_{cd}|^2$ .

Note that the order parameters with a potentially attractive interaction  $U' - J$  are  $[4, 3]$  and  $[5, 2] - [6, 1]$  in  $A_{1g}$ ,  $[5, 1] + [6, 2]$  in  $A_{2g}$ ,  $[5, 2] + [6, 1]$  in  $B_{1g}$ ,  $[5, 1] - [6, 2]$  in  $B_{2g}$ , and finally  $\{[4, 2], -[4, 1]\}$  and  $\{[5, 3], [6, 3]\}$  in  $E_g$ . All these order parameters are associated with spin-triplet states. If we focus first on the largest terms in the normal-state Hamiltonian, namely  $h_{80}$  and  $h_{70}$  (intra-orbital hopping),  $h_{10}$  (inter-orbital hopping), and  $h_{43}$  and  $h_{52-61}$  (atomic SOC), we conclude from Tables S3 and S4 that, among the one-dimensional irreps, the most stable state should be in the  $A_{1g}$  channel since these states are associated with larger entries for  $\hat{F}_A$  and smaller entries for  $\hat{F}_C$ .

Considering now the two-dimensional order parameters, for  $\{[4, 2], -[4, 1]\}$ , we find that the terms stabilizing it, i.e., the ones with the largest contribution to  $\hat{F}_A$ , are  $h_{51+62}$ ,  $h_{52+61}$ , and  $\{h_{42}, -h_{41}\}$ , all associated with momentum-dependent SOC. However, these terms contribute with the same value to the detrimental fitness measure  $\hat{F}_C$ , suggesting that they overall do not favor this pairing state. On the other hand, the two-dimensional order parameter  $\{[5, 3], [6, 3]\}$  is stabilized by  $h_{51+62}$ ,  $h_{52+61}$ , and  $\{h_{53}, h_{63}\}$ . Again, the terms  $h_{51+62}$  and  $h_{52+61}$  contribute with a large value to  $\hat{F}_C$ . On the other hand, the terms  $\{h_{53}, h_{63}\}$  contribute only moderately. This analysis suggests that the  $\{[5, 3], [6, 3]\}$  channel should be the one driving the superconducting instability in the  $E_g$  channel and can be stabilized by large terms  $\{h_{53}, h_{63}\}$ .

From this analysis, we can understand the tendencies observed in the numerical results as follows: the order parameters in  $A_{1g}$ , in particular  $[5, 2] - [6, 1]$ , are strongly stabilized by atomic SOC, in particular by the term  $h_{52-61}$  in the normal-state Hamiltonian, such that reducing the magnitude of this coupling is expected to weaken the superconducting instability in this channel. Moreover, the terms  $\{h_{53}, h_{63}\}$  primarily suppress the order parameter in this channel since their contribution to  $\hat{F}_C$  is larger than the one to  $\hat{F}_A$ . In contrast, the  $E_g$  order parameters, in

Irrep	$[a, b]$	Interac.	$A_{1g}$			$A_{2g}$	$B_{1g}$		$B_{2g}$		$E_g$					
			$h_{80}$	$h_{43}$	$h_{52-61}$	$h_{51+62}$	$h_{70}$	$h_{52+61}$	$h_{10}$	$h_{51-62}$	$h_{20}$	$h_{30}$	$h_{41}$	$h_{42}$	$h_{53}$	$h_{63}$
$A_{1g}$	$[0, 0]$	$U + 2J'$	0	0	0	0	0	0	0	0	0	0	0	0	0	0
	$[8, 0]$	$U - J'$	0	0	24	48	0	48	0	24	12	12	0	0	12	12
	$[4, 3]$	$U' - J$	0	0	8	16	16	16	16	8	4	4	16	16	4	4
	$[5, 2] - [6, 1]$	$U' - J$	11	3	0	32	3	32	3	8	8	8	4	4	8	8
$A_{2g}$	$[5, 1] + [6, 2]$	$U' - J$	11	3	24	8	3	8	3	8	8	8	4	4	8	8
$B_{1g}$	$[7, 0]$	$U - J'$	0	16	8	16	0	16	16	8	4	4	16	16	4	4
	$[5, 2] + [6, 1]$	$U' - J$	11	3	8	8	3	8	3	24	8	8	4	4	8	8
$B_{2g}$	$[1, 0]$	$U' + J$	0	16	8	16	16	16	0	8	4	4	16	16	4	4
	$[5, 1] - [6, 2]$	$U' - J$	11	3	8	32	3	32	3	0	8	8	4	4	8	8
$E_g$	$+ [3, 0]$	$U' + J$	12	4	20	40	4	40	4	20	4	0	4	4	4	16
	$- [2, 0]$		12	4	20	40	4	40	4	20	0	4	4	4	16	4
$E_g$	$+ [4, 2]$	$U' - J$	0	16	8	16	16	16	16	8	4	4	16	0	4	4
	$- [4, 1]$		0	16	8	16	16	16	16	8	4	4	0	16	4	4
$E_g$	$+ [5, 3]$	$U' - J$	12	4	20	40	4	40	4	20	16	4	4	4	0	4
	$+ [6, 3]$		12	4	20	40	4	40	4	20	4	16	4	4	4	0

TABLE S4. Superconducting-fitness measure  $\hat{F}_C$  for the 3D three-orbital model for  $\text{Sr}_2\text{RuO}_4$ . The same notation as in Table S3 has been used.

particular for  $\{[5, 3], [6, 3]\}$ , are primarily stabilized by  $\{h_{53}, h_{63}\}$  since for these terms the contribution to  $\hat{F}_A$  is larger than the one to  $\hat{F}_C$ , while atomic SOC is clearly detrimental. This analysis suggests that by reducing the atomic SOC and enhancing the terms  $\{h_{53}, h_{63}\}$  associated with nonlocal SOC even in momentum, the ground state should change from  $A_{1g}$  to  $E_g$ .

### Effective two-orbital model in the $k_x k_z$ -plane

Sufficiently far from the Brillouin-zone diagonals  $k_y = \pm k_x$ , the bands close to the Fermi energy are dominated by only two of the Ru  $d$ -orbitals. For concreteness, here we consider the  $k_x k_z$ -plane, but our conclusions remain qualitatively valid for general  $\mathbf{k}$ , except close to  $k_y = \pm k_x$ .

In the  $k_x k_z$ -plane, the dominant orbitals at the Fermi energy are  $d_{xz}$  and  $d_{xy}$ . Projecting into this subspace, we obtain an effective two-orbital Hamiltonian which is parametrized by

$$\hat{H}_{2\text{orb}}(\mathbf{k}) = \tilde{h}_{ab}(\mathbf{k}) \tau_a \otimes \sigma_b, \quad (\text{S26})$$

where the  $\tilde{h}_{ab}(\mathbf{k})$  are real functions of momentum,  $\tau_a$  and  $\sigma_b$  are Pauli matrices for  $a, b = 1, 2, 3$  and the  $2 \times 2$  identity matrix for  $a, b = 0$ , encoding the orbital and the spin DOF, respectively. There are, in principle, 16 parameters  $\tilde{h}_{ab}(\mathbf{k})$  but in the presence of time-reversal and inversion symmetries these are constrained to only six, including the term proportional to the identity. The symmetry-allowed terms are listed in Table S5; we classify them in terms of the irreps of  $D_{2h}$ , which is the little group for  $D_{4h}$  in the  $k_x k_z$ -plane. Analogously, we can parametrize the  $s$ -wave gap matrices in the orbital basis as

$$\hat{\Delta} = d_0 \tau_a \otimes \sigma_b (i\sigma_2). \quad (\text{S27})$$

The irreps associated with each  $[a, b]$  combination are the same as for the normal-state Hamiltonian, given in the first two columns of Table S5.

The superconducting-fitness analysis, which is summarized in Table S6, is very much simplified in the two-orbital scenario since the symmetry-allowed matrices form a totally anticommuting set. From the table, one can see that the results concerning  $\hat{F}_A(\mathbf{k})$  and  $\hat{F}_C(\mathbf{k})$  are complementary. Note that the trivial order parameter,  $[0, 0]$ , is stabilized by all the terms in the Hamiltonian while the remaining order parameters of the form  $[a, b]$  need the associated term  $\tilde{h}_{ab}$  in the Hamiltonian to develop a weak-coupling instability. There is an attractive interaction in the orbital-singlet spin-triplet channels  $[2, b]$ . The order parameter  $[2, 1]$  in  $A_g$  is stabilized by the atomic SOC term  $\tilde{h}_{21}$ . The other



Irrep	(a, b)	Type	Basis	Value in $k_x k_z$ -plane	Three-orbital model
$A_g$	(0, 0)	intra-orbital hopping	$1, x^2, y^2, z^2$	finite	(0, 0) in $A_{1g}$
	(3, 0)	intra-orbital hopping			(8, 0) in $A_{1g}$
	(2, 1)	atomic SOC			(6, 1) in $A_{1g}/B_{1g}$
$B_{1g}$	(2, 2)	<b>k</b> -SOC	$xy$	0	(6, 2) in $A_{2g}/B_{2g}$
$B_{2g}$	(2, 3)	<b>k</b> -SOC	$xz$	finite	(6, 3) in $E_g$
$B_{3g}$	(1, 0)	inter-orbital hopping	$yz$	0	(3, 0) in $E_g$

TABLE S5. List of the six symmetry-allowed terms in the effective two-orbital normal-state Hamiltonian  $\hat{H}_{2\text{orb}}(\mathbf{k})$  given by Eq. (S26). For each (a, b), the basis function  $\tilde{h}_{ab}(\mathbf{k})$  should transform according to a specific irrep of  $D_{2h}$  and can be associated with different physical processes (“Type”). The table also gives associated basis functions and provides information on whether they are finite or zero in the  $k_x k_z$ -plane and on the associated term in the original three-orbital model.

			$\hat{F}_A$					$\hat{F}_C$				
			$A_g$	$B_{1g}$	$B_{2g}$	$B_{3g}$		$A_g$	$B_{1g}$	$B_{2g}$	$B_{3g}$	
Irrep	[a, b]	Interac.	$\tilde{h}_{30}$	$\tilde{h}_{21}$	$\tilde{h}_{22}$	$\tilde{h}_{23}$	$\tilde{h}_{10}$	$\tilde{h}_{30}$	$\tilde{h}_{21}$	$\tilde{h}_{22}$	$\tilde{h}_{23}$	$\tilde{h}_{10}$
$A_g$	[0, 0]	$U + 2J'$	1	1	1	1	1	0	0	0	0	0
	[3, 0]	$U - J'$	1	0	0	0	0	0	1	1	1	1
	[2, 1]	<b><math>U' - J</math></b>	0	1	0	0	0	1	0	1	1	1
$B_{1g}$	[2, 2]	<b><math>U' - J</math></b>	0	0	1	0	0	1	1	0	1	1
$B_{2g}$	[2, 3]	<b><math>U' - J</math></b>	0	0	0	1	0	1	1	1	0	1
$B_{3g}$	[1, 0]	$U' + J$	0	0	0	0	1	1	1	1	1	0

TABLE S6. Superconducting-fitness analysis for the effective two-orbital model in the  $k_x k_z$ -plane. The first column gives the irrep of  $D_{2h}$  of the order parameter parametrized by the matrices [a, b] (second column), the third column displays the local interaction in the respective channel, where the potentially attractive channels are highlighted in boldface. Columns 4–8 give the results for the fitness function  $\hat{F}_A$  such that  $\text{Tr } \hat{F}_A^\dagger(\mathbf{k}) \hat{F}_A(\mathbf{k}) = \sum_{cd} (\text{table entry}) |\tilde{h}_{cd}(\mathbf{k})|^2$ , for each term [c, d] in the normal-state Hamiltonian. Analogously, columns 9–13 give the results for the fitness function  $\hat{F}_C$ . We highlight in boldface the  $\tilde{h}_{cd}$  terms which are usually present in 2D models, while the terms in normal typeface describe momentum-dependent SOC or interlayer hopping.

two potentially attractive channels [2, 2] in  $B_{1g}$  and [2, 3] in  $B_{2g}$  are stabilized by  $\tilde{h}_{22}$  and  $\tilde{h}_{23}$ , respectively. Note, however, that  $\tilde{h}_{22}$  is zero in the  $k_x k_z$ -plane (also also in the equivalent  $k_y k_z$ -plane), which should significantly reduce the stability of this state. We are then left with [2, 1] in  $A_g$  and [2, 3] in  $B_{2g}$  as good candidates: For strong atomic SOC  $\tilde{h}_{21}$ , the  $A_g$  channel should be the most stable, whereas for  $\tilde{h}_{23} > \tilde{h}_{21}$ , the  $B_{2g}$  channel becomes the most robust.

We now connect this discussion with the results of the three-orbital analysis above. The order parameter [2, 1] in the two-orbital model corresponds to both [5, 2] – [6, 1] in  $A_{1g}$  and [5, 2] + [6, 1] in  $B_{1g}$  of the three-orbital model, whereas [2, 3] in the two-orbital model corresponds to {[5, 3], [6, 3]} in  $E_g$ . As discussed in the main text, the leading pairing instabilities are in the  $E_g$  and  $A_{1g}$  channels, whereas the  $B_{1g}$  channel is the subleading instability over much of the region where the  $A_{1g}$  channel is dominant. The fact that the  $B_{1g}$  channel is a subleading instability is not surprising, since it must go through a zero as one moves along the Fermi surface from the  $k_x k_z$ - to the  $k_y k_z$ -plane, whereas the  $A_{1g}$  channel maintains a full gap. Since the attractive interactions in both channels are the same, the  $A_{1g}$  state will be favored over  $B_{1g}$ .

The fact that atomic SOC favors the  $A_{1g}$  channel, while increasing the  $\{h_{53}, h_{63}\}$  terms can stabilize an  $E_g$  state, is consistent with the numerical analysis presented in the main text. A naive interpretation of the two-orbital model implies that the  $E_g$  state is stabilized over the  $A_{1g}$  when  $\tilde{h}_{23} > \tilde{h}_{21}$ . However, we numerically find in the full three-orbital model that the condition is closer to  $\{h_{53}, h_{63}\} \gtrsim h_{52-61}/4$ . This discrepancy reflects the fact that the two-orbital model is not valid over the entire Brillouin zone. Nevertheless, the two-orbital model accurately identifies the terms which stabilize the  $E_g$  state over the  $A_{1g}$ .

- 
- [S1] C. N. Veenstra, Z.-H. Zhu, M. Raichle, B. M. Ludbrook, A. Nicolaou, B. Slomski, G. Landolt, S. Kittaka, Y. Maeno, J. H. Dil, I. S. Elfimov, M. W. Haverkort, and A. Damascelli, Phys. Rev. Lett. **112**, 127002 (2014).
- [S2] M. Gradhand, K. I. Wysokinski, J. F. Annett, and B. L. Györfy, Phys. Rev. B **88**, 094504 (2013).
- [S3] T. Scaffidi, J. C. Romers, and S. H. Simon, Phys. Rev. B **89**, 220510 (2014).
- [S4] W. Huang and H. Yao, Phys. Rev. Lett. **121**, 157002 (2018).
- [S5] D. E. King, Journal of Machine Learning Research **10**, 1755 (2009).
- [S6] A. Ramires and M. Sigrist, Phys. Rev. B **94**, 104501 (2016).
- [S7] A. Ramires, D. F. Agterberg, and M. Sigrist, Phys. Rev. B **98**, 024501 (2018)